https://doi.org/10.5194/tc-2019-92
Preprint. Discussion started: 27 May 2019

The Cryosphere
Discussions
Open Access

Toward a coupled model to investigate wave-sea ice interactions in the Arctic marginal ice zone

Guillaume Boutin[1], Camille Lique[1], Fabrice Ardhuin[1], Clément Rousset[2], Claude Talandier[1], Mickael Accensi[1], and Fanny Girard-Ardhuin[1]

[1]Univ. Brest, CNRS, IRD, Ifremer, Laboratoire d'Océanographie Physique et Spatiale, IUEM, Brest, France
[2]Sorbonne Universités (UPMC Paris 6), LOCEAN-IPSL, CNRS/IRD/MNHN, Paris, France

Correspondence: boutinguillaume87@gmail.com

Abstract. The Arctic Marginal Ice Zone (MIZ), where strong interactions between sea ice, ocean and atmosphere are taking place, is expanding as the result of the on-going sea ice retreat. Yet, state-of-art models are not capturing the complexity of the varied processes occurring in the MIZ, and in particular the processes involved in the ocean-sea ice interactions. In the present study, a coupled sea ice - wave model is developed, in order to improve our understanding and model representation of those interactions. The coupling allows us to account for the wave radiative stress resulting from the wave attenuation by sea ice, and the sea ice lateral melt resulting from the wave-induced sea ice break-up. We found that, locally in the MIZ, the waves can affect the sea ice drift and melt, resulting in significant changes in sea ice concentration and thickness as well as sea surface temperature and salinity. Our results highlight the need to include the wave-sea ice processes in models aiming at forecasting sea ice conditions on short time scale, although the coupling between waves and sea ice would probably required to be investigated in a more complex system, allowing for interactions with the ocean and the atmosphere.

1 Introduction

Numerical models exhibit large biases in their representation of the Arctic sea ice concentration and thickness, regardless of their complexity or resolution (Stroeve et al., 2014; Chevallier et al., 2017; Wang et al., 2016; Lique et al., 2016). Comparing 10 reanalyses based on state-of-the-art ocean-sea ice models against observations, Uotila et al. (2018) found that the model biases are the largest in the Marginal Ice Zone (MIZ). Indeed, the MIZ is characterized by a wide variety of processes resulting from the highly non linear interactions between the atmosphere, the ocean and the sea ice (Lee et al., 2012), and many of these processes are only crudely (if at all) taken into account in models. Some of these processes result from the interactions between surface wave and sea ice, and are thought to be key for the dynamics and evolution of the MIZ (Thomson et al., 2018). These interactions are the focus of the current paper.

Summer sea ice in the Arctic has been drastically receding over the past few decades (Comiso et al., 2017), resulting in an expansion of the MIZ which is expected to be intensified in the future (Aksenov et al., 2017). This offers an expanding fetch for waves to grow and propagate (Thomson and Rogers, 2014), suggesting an overall increase of wave heights in the Arctic (Stopa et al., 2016b). Once generated, waves can then propagate into sea ice, impacting strongly the dynamical and thermodynamic sea ice properties in the MIZ through different mechanisms (Asplin et al., 2012). First, observations suggest that waves determine the shape and size of the sea ice floes in the MIZ, through the break-up occurring when the ice cover is deformed (Langhorne et al., 1998), or by controlling the formation of frazil/pancake ice (Shen and Ackley, 1991). Wave-induced sea ice fragmentation is also expected to affect lateral melt (Steele et al., 1992), heat fluxes between ocean and atmosphere (Marcq and Weiss, 2012), or sea ice drift in the MIZ (McPhee, 1980; Feltham, 2005; Williams et al., 2017). When breaking in the MIZ, waves can generate turbulence in the mixed layer (Sutherland and Melville, 2013), possibly affecting the rate of ice formation or melting by modulating heat fluxes between the ocean, the sea ice and the atmosphere. Observations conducted during a storm in October 2015 in the Beaufort Sea have for instance revealed that storm-induced waves can lead to an increase of surface mixing and an associated heat entrainment from upper ocean, resulting in an important melt of pancake ice (Smith et al., 2018). Finally, waves transport momentum, so that when they are attenuated in the MIZ through reflection or dissipation, part of the momentum goes into sea ice. This process, called the wave radiative stress (WRS; Longuet-Higgins and Stewart, 1962; Longuet-Higgins, 1977), acts as a force that pushes the sea ice in the direction of the propagation of the attenuated waves. This force is a dominant term in the ice momentum balance on the outskirts of the Southern ocean sea ice (Stopa et al., 2018b) and it may become more prominent in the Arctic. In return, sea ice strongly attenuates waves propagating in the MIZ, either by dissipative processes (e.g. under-ice friction, inelastic flexure, floe-floe collisions) or conservative processes (e.g. scattering) (Squire, 2018).

Most of the recent efforts in the modeling community have been focusing on the impact of sea ice on waves, leading to the development of wave models accounting for the presence of sea ice (Dumont et al., 2011; Williams et al., 2013; Montiel et al., 2016; Boutin et al., 2018). By prescribing sea ice conditions, these models are able to reproduce accurately the time and space variations of wave height in sea ice retrieved from recent field observations (Kohout et al., 2014; Thomson et al., 2018; Cheng et al., 2017) and innovative processing of Synthetic Aperture Radar (SAR) satellite observations (Ardhuin et al., 2017). The good agreement with the observations also suggests a proper representation and quantification of the wave attenuation and propagation in sea ice in these models (Ardhuin et al., 2016; Rogers et al., 2016; Ardhuin et al., 2018). Yet, in this case, sea ice conditions are only a forcing and thus not affected by waves. This means that these models cannot realistically represent the fate of the sea ice floes once broken by waves, as they do not account for advection, melting and refreezing processes. A first step toward the representation of the wave-sea ice interactions was done by Williams et al. (2013) and Boutin et al. (2018), who included in their respective model a Floe Size Distribution (hereafter FSD) that evolves depending on the sea state. Yet, considering only the sea ice fragmentation is not sufficient to represent the full complexity of the wave-sea ice interactions.

In contrast, little progress has been done regarding the inclusion of the effects of waves in coupled ocean-sea ice models. Using a very simple parameterization, Steele et al. (1989) and Perrie and Hu (1997) have investigated the effect of WRS on the sea ice drift in the MIZ, only considering the attenuation of waves generated between the ice floes. They found a limited impact on the sea ice conditions. More recently, Williams et al. (2017) have implemented a wave module in the semi-lagrangian sea ice model neXtSIM (Rampal et al., 2016) and found that high waves conditions can induce a significant displacement of the sea ice edge. The implementation of FSDs in different sea ice models as done by Zhang et al. (2015) or Horvat and Tziperman (2015) has also allowed the assessment of the potential enhancement of lateral melt by wave-induced ice fragmentation (Zhang et al., 2016; Bennetts et al., 2017), but the representation of waves remains too crude to simulate the full effect of waves on the evolution of sea ice.

In the present study, we go beyond the simple inclusion of the forcing of wave by sea ice or of sea ice by wave in models, by proposing a full coupling between a spectral wave model and a state-of-art sea ice model. The coupled framework allows us to investigate the interactions between waves and sea ice in the Arctic, and the impact that including these effects in a model has on the representation of the wave, ocean, and sea ice properties in the Arctic MIZ. The remainder of this paper is organized as follows. The different models and configurations used in this study are described in Section 2. Section 3 is devoted to the theoretical and practical implementation of the coupling between the two models. In section 4, we compare pan Arctic simulations in which the coupling between wave and sea ice is implemented or not, in order to quantify the dynamical and thermodynamical impacts on the coupling on the sea ice and ocean surface properties. A summary and conclusions are given in Section 5.

2 Methods

In this study we make use of the spectral wave model WAVEWATCH III® (hereafter WW3; The WAVEWATCH III ® Development Group, 2016), building on the previous developments performed by Boutin et al. (2018) who included a FSD in WW3 as well as a representation of the different processes by which sea ice can affect the propagation and modulation of waves in the MIZ. We also use the sea ice model LIM3 (Vancoppenolle et al., 2009; Rousset et al., 2015), in which a FSD is first implemented as described in Section 3.2. The two models are coupled through the coupler OASIS-MCT (Craig et al., 2017). Two configurations of different complexities are used in the following and briefly described in the remaining of this section.

2.1 Idealized configuration

In order to test and illustrate the effect of the coupling (Section 3), we make use of a simple idealized configuration (see Fig. 1), in which LIM3 is used in a stand alone mode (without any ocean component). The configuration is a squared domain with 100×100 grid cell, with a resolution of 0.03^o in both directions (corresponding roughly to 3 km). Both models are run on the same grid, and with the same time step set to 300s. The coupling time step is set to 300s too. The sea ice is only forced by waves, without any wind or ocean current. Following Boutin et al. (2018), the simulation starts at rest, with distributions of sea ice concentration (Fig. 1a) and thickness (Fig. 1c) set to represent roughly the conditions that can be found in the MIZ. Starting from the western border, the domain is free of ice over the first $\simeq$10 km, after which the ice concentration c increases linearly from 0.4 to 1 about 90 km further eastward (longitude=0.84^oE). Ice thickness also increases from west to east following $h_i = 2(0.1 + \mathrm{e}^{-N_x/20})$, where N_x is the number of grid cells in the x direction starting from the western border of the ice covered domain. Waves radiate from part of the western border of the domain, between 1.2 and 1.8^o of latitude, and propagate to the east. The wave spectrum at the boundary is extracted from an Arctic realistic simulation using WW3 described by Stopa et al. (2016a) for May 2nd and 3rd, 2010, during which a storm happened south of Svalbard (Collins et al., 2015). Here we rotate the spectrum so that the direction with the largest density of wave energy is lined up with our x-axis. Simulations start on April 30th, at 02:00 a.m., and the attenuation processes (scattering, bottom friction and inelastic dissipation) use the same parameterization as in the reference simulation described by Ardhuin et al. (2018).

2.2 Pan-Arctic configuration

We also make use of the CREG025 configuration (Dupont et al., 2015; Lemieux et al., 2018), which is a regional extraction of the global ORCA025 configuration developed by the Drakkar consortium (Barnier et al., 2006). Although the coupling is solely between the LIM3 and WW3, the configuration here also includes the ocean component of NEMO 3.6 (Madec, 2008). CREG025 encompasses the Arctic and parts of the North Atlantic down to 27^o, and has 75 vertical levels and a nominal horizontal resolution of $1/4^o$($\simeq$ 12 km in the Arctic basin). Both NEMO-LIM3 and WW3 are run on the same grid. Initial conditions for the ocean are taken from the World Ocean Atlas 2009 climatology for temperature and salinity. The initial sea ice thickness and concentration are taken from a long ORCA025 simulation performed by the Drakkar Group. Along the lateral open boundaries, monthly climatological conditions (comprising sea surface height, 3-D velocities, temperature and salinity) are taken from the same ORCA025 simulation. Regarding the atmospheric forcing, we use the latest version of the Drakkar Forcing Set (DFS 5.2, which is an updated version of the forcing set described in Brodeau et al., 2010). The choices regarding the parameterization of the wave-ice attenuation are following the ones made in the *REF* simulation by Ardhuin et al. (2018). The value of the ice flexural strength has however been increased from 0.27 MPa to 0.6 MPa, which is the highest value used in Ardhuin et al. (2018). This choice makes sea ice harder to break, and aim at compensating the fact that no lateral growth of sea ice is included in our coupled framework.

Three simulations are performed. First we run a simulation based solely on NEMO-LIM3 (referred to as NOT_CPL), covering the period from January 1st, 2002 to the end of 2010, in which the lateral melt parameterization from Lüpkes et al. (2012) is activated. The first years of the simulations are allowing for the adjustment of the ocean and sea ice conditions and we only analyze results from August and September 2010. During that period, the sea ice extent reaches its annual minimum, providing some fetch for the generation of sea ice, and in particular in the Beaufort Sea. The model sea ice extent during the summer of 2010, and more generally the distribution of the sea ice concentration, compares reasonably well with satellite observations (not shown. Note that this period includes a drop in sea ice concentration in the Central Arctic, found both in model results and in satellite observations, that has already been documented by Zhao et al. (2018) and attributed to an enhancement of ice divergence in this region this particular year. This specific period has also been chosen as some storms occurred during it, so that extreme waves conditions can be investigated. Another simulation (CPL) is initialized from NOT_CPL on August 1st 2010 and run until September 9th 2010. After that date, sea ice extent starts to increase again, and as our FSD distribution does not allow for the refreezing of the sea ice floes, we cannot represent realistically the processes at play during that period.

Finally, we run a simulation over the same period, based solely on WW3 (referred to WAVE), in which the wave model is forced by sea ice conditions from the NOT_CPL simulation. In order to allow for some spin up for the waves to develop and break the ice, we remove the first 3 days. In the following, all the results are for the 37-days period between August 4th and September 9th 2010.

3 Implementation of the coupling between the wave and the sea ice models.

The objective of this section is to present the theoretical background and the practical implementation of the coupling between LIM3 and WW3. Fig. 2 shows the principle of the coupling and the variables that are exchanged between the two models. Briefly, LIM3 provides sea ice floe size, thickness and concentration to WW3 in order to estimate the wave attenuation and wave-induced sea ice break-up. Note that LIM3 being a multi-category sea ice model, the actual state variable is a sea ice thickness distribution g_h, from which the mean sea ice thickness can be defined either by doing a grid-cell average or by doing an ice-cover average. Here we choose to exchange the ice-cover average sea ice thickness, although this choice does not affect significantly our results. WW3 then returns the WRS to LIM3, as well as the updated floe size. LIM3 takes into account the WRS in its ice transport equation, and advects the sea ice and its information on floe size. If break-up has occurred in the wave model, floe size is actualized to match the FSD assumed in WW3. The floe size is then used to estimate lateral melt.

In the following, we describe in more details the modifications that have been done in LIM3 and WW3 in order to couple them, and how variables are exchanged between the two models. The coupling allows a new formulation for the sea ice lateral melt in LIM3 (section 3.3).

3.1 Wave Radiative Stress

Waves transport momentum, and when they are attenuated either by dissipation or reflections, this momentum is transferred to the cause of this attenuation (Longuet-Higgins, 1977). In the case of sea ice, this momentum loss thus acts as a stress that pushes sea ice in the direction of attenuated waves. Following the study of Williams et al. (2017), in which a WRS was implemented in neXtSIM, the WRS $\tau_{w,i}$ is computed as:

$$\tau_{w,i} = \rho_w g \int_0^{\infty}\int_0^{2\pi} \frac{S_{\text{ice}}(\mathbf{x};\omega,\theta)}{\omega/k}(\cos\theta, \sin\theta)\,d\theta d\omega \tag{1}$$

where ρ_w is the water density, g is gravity, ω, θ and k are respectively the radial frequency, direction and wavenumber of waves and $S_{\text{ice}}(\mathbf{x};\omega,\theta)$ is the source term corresponding to wave attenuation by sea ice at a given position.

Once estimated by WW3, the WRS is then sent to the sea ice model and added as an additional term in the momentum equation of LIM3 (Rousset et al., 2015):

$$mD_t\mathbf{u} = \nabla\cdot(\boldsymbol{\sigma}) + c(\tau_a + \tau_o) + \tau_{w,i} - mf\,\mathbf{k}\times\mathbf{u} - mg\nabla\eta, \tag{2}$$

in which m is the total mass of ice and snow per unit of area, $\mathbf{u}$ is the ice velocity vector, $\boldsymbol{\sigma}$ is the internal stress tensor, f is the Coriolis parameter, η is the sea surface elevation, c is the ice concentration, and τ_a, τ_o are the atmospheric and oceanic stresses, respectively. In contrast to τ_a and τ_o, $\tau_{w,i}$ doesn't require to be multiplied by c, since the partial sea ice cover is already accounted for in WW3.

Fig. 1 illustrates the effect of the implementation of the WRS in our simple model. Here, the sea ice thermodynamics is switched off, so that we only simulated the effect of waves pushing sea ice. Under the action of waves, the sea ice edge shifts eastward, resulting in an increase of the sea ice concentration (panel b). As the sea ice near the sea ice edge is compacted, it creates a sharp gradient in sea ice concentration and thickness (panels b,e). When comparing panels (e) and (f), it is clear that wave attenuation also responds to this change of the sea ice properties: waves tend to penetrate further eastward when the sea ice edge retreats to the east, but are then attenuated faster in the compacted sea ice.

3.2 Floe size distribution and sea ice break-up

As mentioned earlier, waves can break sea ice and thus impact the sea ice floe size. It is thus required to exchange a FSD between the two models. A FSD has been previously implemented in WW3 by Boutin et al. (2018), and is used to estimate the wave attenuation due to inelastic flexure and scattering. Following the work by Toyota et al. (2011) and Dumont et al. (2011), we assume that the FSD in WW3 follows a truncated power law between a minimum floe size, $D_{\min}$ and a maximum floe size, $D_{\max}$. $D_{\min}$ corresponds to the minimum floe size that can be generated by waves and is of the order of $O(10\mathrm{m})$, while $D_{\max}$ depends on the local waves properties and is used to estimate the level of sea ice fragmentation.

There is no FSD included in the standard version of LIM3. However, recent work by Zhang et al. (2015) and Horvat and Tziperman (2015) have proposed ways to implement a FSD in sea ice models, following what is done for the sea ice thickness distribution (which is a state variable of any multi category sea ice model). Here we start by following the approach of Zhang et al. (2015), distributing ice concentration into bins corresponding to different floe sizes by defining a FSD function g_D. The evolution of the FSD depends on sea ice advection, thermodynamics and mechanical processes, and is given by:

$$\frac{\partial g_D}{\partial t} = -\nabla \cdot (\mathbf{u} g_D) + \Phi_{th} + \Phi_m, \tag{3}$$

in which $\mathbf{u}$ corresponds to the sea ice velocity vector, Φ_{th} is a redistribution function of floe size due to thermodynamic processes (*i.e* lateral growth/melt), and Φ_m is a mechanical redistribution function associated with processes like fragmentation, lead opening, ridging, and rafting. In their sea ice model neXtSIM, Williams et al. (2017) have implemented a FSD that enables the floes to be advected once they have been broken by waves, making the assumption that the FSD follows a truncated power-law between a minimum and a maximum floe size, similarly to the assumption made in WW3. Here we take a similar approach and implement a FSD in LIM3 that evolves following eq.(3). Yet, in contrast to Williams et al. (2017), we do not make any assumption on its shape in general, but the FSD is forced to follow the power-law assumed in WW3 as soon as wave-induced sea ice break-up occurs. This ensure coherence between the FSDs in LIM3 and WW3. We acknowledge that this assumption on the FSD is strong, and as discussed in Roach et al. (2018a), it is not a suitable way to proceed when studying the sea ice evolution, since the FSD should evolve freely and observation have regularly shown that power-law distributions are not always followed (e.g. Inoue et al., 2004). However, understanding the details of the FSD evolution is beyond the scope of this study, and assuming a power-law FSD is coherent with a distribution caused by a succession of break-up event (Toyota et al., 2011; Dumont et al., 2011). The details of the mechanical redistribution function Φ_m are mostly following what has been proposed by Zhang et al. (2015) and are given in appendix A.

Now that both models include a FSD, the coupling between the two models can be done in order to represent the effect of the wave-induced sea ice break-up, whose occurrence in LIM3 is determined depending on information provided by WW3. As mentioned earlier, sea ice break-up in WW3 is controlled by local wave properties and break-up events result in an update of the maximum floe size $D_{\max}$. It is thus logical to define a similar parameter $D_{\max,\mathrm{LIM3}}$ from the LIM3's FSD, that would ideally equals $D_{\max}$. Yet estimating $D_{\max,\mathrm{LIM3}}$ is not straightforward. Indeed, our FSD implementation requires that $D_{\max,\mathrm{LIM3}}$ corresponds to the upper limit of the power law followed by the FSD in both WW3 and LIM3, but also that $D_{\max,\mathrm{LIM3}}$ can evolve with the deviations of the LIM3's FSD from this power-law under the effects of sea ice advection and thermodynamics. Calling $g_{D,\mathrm{P.L}}$ the distribution corresponding to a FSD following the assumed power-law, we thus define $D_{\max,\mathrm{LIM3}}$ as the greatest value of D for which the following condition applies:

$$\int_{D}^{\infty} g_D dD \geq k_{D_{\max}} g_{D,\mathrm{P.L}}, \tag{4}$$

in which $k_{D_{\max}}$ is an *ad hoc* parameter allowing the value of $D_{\max,\mathrm{LIM3}}$ to remain unchanged when the FSD slightly deviates away from the assumed power-law (after lateral melt or advection for instance). Setting $k_{D_{\max}}$=1 is a too strong constraint, and results in noisy $D_{\max}$ distributions, since the smallest change in the FSD after a break-up event results in a change of $D_{\max,\mathrm{LIM3}}$. Values between 0.5 and 0.8 lead to smoother FSDs, but overall the choice of $k_{D_{\max}}$ does not significantly affect our results. In the following, $k_{D_{\max}}$ is set to 0.5.

Floes that have never been broken by waves have no physical reason to follow this truncated power-law. In practice, if we consider a discrete number N of floe size categories, the N^{th} category should represent these unbroken floes, with a different condition to set the value of $D_{\max,\mathrm{LIM3}}$ to D_N (the upper size limit of this category). We thus consider that sea ice in a grid cell can be qualified as unbroken only if most of its floes belongs to this N^{th} category, so that $D_{\max,\mathrm{LIM3}} = D_N$ only if $g_N > 0.5c$, g_N being the value of the FSD function associated to the N^{th} category and c the total sea ice concentration.

In all our simulations, sea ice is initialized as unbroken everywhere, so that $g_N = c$, and $D_{\max,\mathrm{LIM3}} = D_N$. As soon as wave-induced break-up occurs, $D_{\max,\mathrm{LIM3}}$ is updated. To do so, the received value of $D_{\max}$ is rounded up to the upper limit of the category it lies in. $D_{\max,\mathrm{LIM3}}$ is therefore slightly greater than the value received from WW3, with an error that depends on the width of its associated floe size category.

Tests on the simplified domain were also performed to investigate the sensitivity of the results to the number and width of floes categories. This sensitivity remains really small as long as the widths of the categories are smaller than 10 m and that the categories cover a range of floe sizes larger than 300 m. In the following, we used N =60 floe size categories, that we define following the conditions:

- A first category corresponding to the sea ice floes that are already broken but cannot be broken anymore [$D_0 = 8$ m, $D_1 = 13$ m]. D_0 represents the smallest floe size possible in the model, and is set to 8 m in order to agree with the minimum floe size used in LIM3 to estimate lateral melt from the parameterization by Lüpkes et al. (2012). D_0 is also of the same order than the size of the smallest floes that can be generated by wave-induced break-up (Toyota et al., 2011) and therefore an acceptable value for the lower limit $D_{\min}$ that the truncated power-law is assumed to follow after wave-induced break-up.
- 58 categories for which $D_n - D_{n-1} = 5$ m, with $1 \leq n \leq N-1$.
- A last category representing unbroken floes [$D_{N-1} = 298$ m, $D_N = 1000$ m]. This value of 1000 m was set as it is one order of magnitude higher that the floe size generated by waves (Toyota et al., 2011).

We evaluate the effect of this part of the coupling between WW3 and LIM3, as well as the robustness of the implementation of the FSD in LIM3, by performing 2 simulations in our idealized configuration, based on WW3 only or the coupled WW3-LIM3 model (Fig. 3). Thermodynamics is still switched off in the WW3-LIM3. The comparison between $D_{\max}$ estimated from the WW3 simulation and $D_{\max,\mathrm{LIM3}}$ from the coupled framework is shown on Fig. 3(a,b,c). The pattern of broken sea ice is broadly similar in the two simulations (a,b), despite the sea ice retreat due to the WRS in the coupled case. Differences in $D_{\max}$ (Fig. 3c) follow the wave heights differences already commented on Fig. 1(e,f). Indeed, the retreat of the ice edge due to the WRS allows for waves to propagate further with less attenuation, thus involving more sea ice break-up and a lower maximum floe size close to the open ocean in the coupled simulation. Further east in the MIZ, the sea ice compacted by the WRS effect generates stronger wave attenuation, and thus less sea ice fragmentation and a greater maximum floe sizes when compared to the not-coupled simulation. Both effects partly compensate, so that the shift in the ice edge position affects very little the extent of broken ice, which is almost unchanged between the two simulations. Fig. 3d shows the FSD at two locations in the domain. At both locations, the distribution of ice covered area within the different categories agrees very well between LIM3 and the truncated power-law assumed in WW3. The area covered by floes of the smallest possible size in LIM3 is nevertheless greater than it would be if the FSD was exactly following the truncated power-law. This is because floes that have been broken to the smallest possible size do not contribute to the redistribution (see section A) and accumulate in this category since no lateral growth occurs. Note that a coupled simulation in which advection had been deactivated was also run to ensure that, in a case with unaffected initial sea ice properties, no significant discrepancies were noticeable for both significant wave height and maximum floe size between an coupled and a not-coupled simulation (not shown).

3.3 Lateral melt

A parameterization to account for the sea ice lateral melt is already implemented in LIM3. Its formulation follows Steele (1992):

$$\frac{dc}{dt} = -w_{\mathrm{lat}} \frac{\pi}{\alpha \langle D \rangle} c, \tag{5}$$

where c is the sea ice concentration, w_{lat} is a lateral melt rate, which depends on the difference between sea ice and sea surface temperatures taken from Maykut and Perovich (1987), and α is a coefficient which varies with the floe geometry. By default, $\alpha = 0.66$, which is the average value of the non-circularity of floes obtained by Rothrock and Thorndike (1984). $\langle D \rangle$ represents the average floe size (referred to as the caliper diameter). Based on an number of observations, Lüpkes et al. (2012) fitted a relationship between $\langle D \rangle$ and sea ice concentration, so that the lateral melt in the model can be estimated depending only on sea ice concentration. This relationship finds a value of $\langle D \rangle$ that increases very little from its minimum value (set to D_0) as long as the sea ice concentration remains lower than $\simeq 0.6$ (see Fig. 3 from Lüpkes et al., 2012). It might be a problem far from the ice edge, where divergence can make the ice concentration decreasing to 0.6 or below with an actual floe size being much greater than $\simeq 10$ m. In the following, we refer to this lateral melt parameterization as the parameterization of Lüpkes et al. (2012), although we acknowledge that the work of Lüpkes et al. (2012) only provides a relationship between the average floe size and the sea ice concentration.

In the case of our coupled model, we estimate a FSD, and it thus makes sense to implement a parameterization of the lateral melt that depends explicitly on the FSD rather than the sea ice concentration. Following the work by Horvat and Tziperman (2015) and Roach et al. (2018a), we estimate the lateral melt as:

$$\frac{dc}{dt} = \int_{0}^{\infty} \Phi_{th} dD = \int_{0+}^{\infty} -w_{\mathrm{lat}} \left(-\frac{\partial g_D}{\partial D} + \frac{2}{D} g_D \right) dD \tag{6}$$

where Φ_{th} is the change in area covered by floes of a size D due to lateral melt (see Eq.3). Note that lateral melt for floes in the unbroken category is computed assuming that all the floes have a size D of 1000 m.

We run two simulations, in which the lateral melt is either estimated from the formulation of Lüpkes et al. (2012), or by our new formulation, which accounts for the actual FSD that is determined by both the sea ice and the wave models (Fig. 4). Here we only activate the lateral melt, and turn off the basal and surface melt. The sea surface temperature is set constant to $T = 0.3^o C$. Floe size categories are the same as in 3.2. In the case of the Lüpkes et al. (2012) parameterization (Fig. 4a), the lateral melt only depends on the sea ice concentration and thus follow its distribution. In the second case (Fig. 4b), lateral melt is highly constrained by both the distribution of sea state and ice properties, and is only significant where the sea ice is broken. Melt rates are overall higher when estimated from the Lüpkes et al. (2012) parameterization, mostly due to the fact that the average floe size in the non coupled run is very close to D_0 for a wide range of concentrations. Unlike the parameterization that we propose here, the parameterization of Lüpkes et al. (2012) results in a significant lateral melt far from the ice edge, where sea ice is mostly compact and unbroken, which is likely unphysical.

4 Importance of wave-sea ice interactions.

In this section we compare the three simulations performed with the CREG025 configuration described in Section 2.2, in order to quantify the impact of the including the wave-sea ice interactions for the waves, sea ice and ocean surface properties. Remember that although the coupling is only between the wave and the sea ice components, our coupled model includes an ocean component, which is only interacting with the sea ice model but not the wave model. This means that we only consider here the impact that waves may have on the ocean through their impact on the sea ice conditions.

To evaluate the impact of waves in the MIZ, we first need to define the MIZ in our model. Various criteria, relying either on sea ice concentration, floe size or the region where waves impact the sea ice floe size, have been previously used to delimit the MIZ (see for instance Dumont et al., 2011; Strong and Rigor, 2013; Sutherland and Dumont, 2018). Here we take the following definition based on the maximum floe size: $0 < \langle D_{\max} \rangle < 700$ m, where $< \langle D_{\max} \rangle$ is the average of the maximum floe size over the studied period. Physically, it roughly corresponds to the region where sea ice has been broken during a time period that is long enough for the averaged maximum floe size to be under 1000 m (which is the limit between the broken and unbroken ice). Note that our results are not dependent on the definition of the MIZ.

4.1 Effect of the coupling at the pan-Arctic scale

4.1.1 Impact on the wave properties

First, we examine the significant wave height H_s in the CPL and WAVE simulations (Fig. 5(b,e)). Differences in H_s between the two simulations are small, not exceeding $\simeq$ 15 cm on average. Moreover, the two runs exhibit similar patterns of $D_{\max}$, indicating that the wave-induced break-up is similar in the two simulations (Fig. 5f). Locally, in the Barents and Greenland seas for instance, the differences of $D_{\max}$ can be significant, due to the specific ice drift conditions in these regions. Indeed, the overall southward drift of sea ice tends to bring unbroken sea ice from the central Arctic to regions where sea ice is broken up, increasing $D_{\max}$ in the CPL simulation. The signs of the differences in H_s and $D_{\max}$ vary regionally. This might be due to the differences in sea ice concentration and thickness, as the wave attenuation in sea ice is very sensitive to sea ice properties (see for instance Ardhuin et al., 2018). Indeed, the pattern of the differences in H_s between the CPL and WAVE runs is consistent with the differences in sea ice concentration and thickness between the CPL and the NOT_CPL simulations (Fig. 6). One should keep in mind that the sea ice conditions from the NOT_CPL run are used as forcing for the WAVE run), with higher waves found in regions where ice is less concentrated and thinner.

4.1.2 Impact on the sea ice and sea surface properties

We now focus on the effect of adding a wave component for the sea ice properties, by comparing results from the CPL and NOT_CPL simulations. Fig. 6 shows the Pan-Arctic distribution of the sea ice thickness and concentration averaged over the 37 days considered in the CPL simulation, as well as the differences with the NOT_CPL simulation. These differences are concentrated in the vicinity of the ice edge and exhibits different signs depending on the location. Positive and negative anomalies tend to compensate, resulting in weak overall difference in sea ice extent and volume when averaging over the full Arctic Basin. If we only consider the MIZ, the sea ice volume and area decrease by about 3% and 2%, respectively, between CPL and NOT_CPL (Fig. 7b). Locally, however, these variations can be much larger. In the MIZ of the Beaufort Sea for instance, the relative changes can be as high as 10% for mean sea ice thickness.

There are also difference in sea surface properties between the two simulations (Fig. 8), with an average increase in sea surface temperature (SST) and salinity (SSS) in the MIZ of the order as high as $0.5^{o}C$ and 0.8 psu locally, respectively. It is worth noting that, in contrast to the sea ice properties, the sign of the differences in SST and SSS tends to be positive, i.e. warmer and saltier in the CPL experiment compared to the NOT_CPL one.

4.1.3 Thermodynamical effect of the coupling

Given that there is no coupling between the ocean and the wave components, the difference in sea surface properties must arise from variations in sea ice conditions, and in particular the sea ice melt, that we investigate further. Fig. 9(a,b) shows the total sea ice volume melted laterally during the studied period in the CPL run as well as its difference with the same quantity from the NOT_CPL run. The sea ice volume melted by lateral melt shows very similar spatial patterns between the two simulations, although it is estimated from two very different parameterizations (Eq. 5 and Eq. 6), although lateral melt estimated by the parameterization from Lüpkes et al. (2012) tends to be larger in NOT_CPL. The difference is substantial, the sea ice volume melted in the MIZ in NOT_CPL being 30% larger than in CPL (7a). Another signal is found in the central Arctic, where the value of lateral melt in the NOT_CPL run are small but positive. This is due to the drop in sea ice concentration that happens in the region in August 2010 (Zhao et al., 2018), resulting in a reduction of the average floe size below 100 m when estimated by the formulation of Lüpkes et al. (2012) and thus triggering some lateral melt. In contrast, the absence of waves in the middle of the sea ice pack in the coupled simulation results in unbroken ice in this region, and therefore no lateral melt. An average floe size of $\simeq$ 100 m in the middle of the pack seems somewhat unrealistic, and highlights the limitation of the parameterization of Lüpkes et al. (2012) when used in Pan-Arctic configurations. This lateral melt enhancement in the central Arctic in the NOT_CPL simulation amplifies the decrease of sea ice concentration in this region. The combination of the sea ice concentration decrease and lateral melt in the NOT_CPL simulation therefore explains the deficit in sea ice concentration reported in the central Arctic when compared to the coupled simulation (Fig. 6b). Moreover, the differences in lateral melt between the two simulations being mostly negative, it cannot explain the regional patterns found in the distribution of sea ice properties differences.

Fig. 9(c,d) shows the differences in bottom and total ice melt, between the CPL and NOT_CPL simulations. The spatial pattern of the differences in bottom and total ice melt are very similar, meaning that the variations in bottom melt dominate the differences in sea ice melt between CPL and NOT_CPL, although the bottom melt is computed the same way in the two simulations. This result is confirmed by rerunning a coupled and an uncoupled simulation of NEMO-LIM3 while de-activating lateral melt (not shown), which yields differences in total melt distribution almost identical to the ones presented on Fig. 9(c,d).

The total sea ice volume melted once integrated over the MIZ increases by 3% between CPL and NOT_CPL, mainly due to the larger volume of sea ice melted laterally in NOT_CPL (Fig. 7a). In parallel, bottom melt slightly decreases by $\simeq$1% between these two simulations. This result does not reflect the fact that the regional differences of total melt are dominated by bottom melt. An explanation is that bottom and lateral melt depend both on the available heat in the surface layer, either directly for bottom melt, or indirectly through lateral melt that depends on the SST. If lateral melt occurs, it removes heat from the surface layer, therefore reducing the bottom melt capacity. Oppositely, if this heat is not used for lateral melt, it remains available for bottom melt. The overall decrease of bottom melt in the MIZ between CPL and NOT_CPL visible on Fig. 7a therefore mostly results from the compensation of the increase of lateral melt due to the change of parameterization, as can be seen on Figs. 9b and 9c. Actually, in contrast to what was found in previous studies by Zhang et al. (2016); Bennetts et al. (2017); Roach et al. (2018a), de-activating completely lateral melt in both runs (not shown) has a negligible effect on the quantity of melted ice in our simulations (not shown).

4.1.4 Dynamical effect of the coupling

The differences in lateral melt between the CPL and the NOT_CPL runs cannot explain the differences in sea ice and sea surface properties seen on Figs. 6 and 8. We thus investigate the impact of the WRS on the sea ice conditions and melt. Fig. 9(e,f) show the mean directions of the wind stress and the WRS in the CPL simulation and the ratio of WRS magnitude on wind stress respectively. This ratio is generally low, not exceeding 15% of the wind stress in the eastern Barents Sea, where the WRS reaches its highest magnitude. This is much smaller than the values retrieved from satellite observations in the Southern Ocean, where the wind stress and the WRS can be of comparable magnitudes (Stopa et al., 2018a). It is also worth noting that the regions where this relative importance of the WRS compared to the wind is large do not always coincide with regions where differences in sea ice properties are significant (Fig. 6). In the Beaufort Sea for instance, there is substantially less sea ice melt in the CPL simulation than in the NOT_CPL one, although the ratios of WRS over the wind stress are only of the order of a few percents (Fig. 9f). The opposite situation is visible in the Barents Sea, where the high relative influence of the WRS does not result in a significant increase of the sea ice melt when the effect of the waves is included. Therefore, the amplitude of the WRS alone does not allow to conclude on the mechanism through which the WRS impact sea ice melt. In the Southern Ocean, Stopa et al. (2018a) found that the orientation of the WRS, that tends to be orthogonal to the sea ice edge, might explain why WRS might be as important as the wind (that tends to vary much more its direction over time) to determine the position of the sea ice edge. Similarly, here, we found that the WRS is very often orientated orthogonally to the ice edge, towards packed ice. It is due to the fact that the longer waves encounter sea ice on their path, the more they are attenuated. The direction of propagating waves at a given point in sea ice is then generally imposed by the waves that have traveled the shortest distance in sea ice. This is particularly visible in some part of the Greenland and the Kara seas, where wind and wave stresses have opposite direction on average. In the Chukchi and the eastern Beaufort seas, the WRS is orthogonal to the wind stress. In contrast, in the Laptev sea, the directions of the WRS and the wind stress roughly align, and thus play together in setting the position of the sea ice edge in the CPL run. However, at the pan-Arctic scale, there is no clear relationship between the WRS direction and the differences in sea ice melt induced by the WRS in the CPL simulation.

The primary effect of the WRS is to push sea ice, modifying the intensity and the direction of the sea ice drift. This impact is significant in the MIZ, where the averaged sea ice drift velocity increases by $\simeq$9% between the CPL and the NOT_CPL runs (Fig. 7b). This overall increase of the sea ice velocity can be explained by the fact that both WRS and sea ice drift have a dependency on wind direction. As it was the case for sea ice thickness and concentration, the distribution of the differences in sea ice drift velocity between the two simulations varies strongly depending on the region considered (not shown), but exhibits no clear relationship at the Pan-Arctic scale that could explain the differences in sea ice melt induced by the WRS.

In the following we investigate in further details the wave-sea ice interactions in two regions during storms. Indeed, although the differences between the CPL and NOT_CPL run at the pan-Arctic scale remains small, it is clear that the way the waves can influence the sea ice and the ocean surface would depend on the local properties of wave, wind, sea ice and ocean surface.

4.2 Regional impacts of waves-sea ice interactions during storm events

4.2.1 Case 1: Storm in the Beaufort Sea (16-17 August 2010)

We first focus on a storm event that occurred near the MIZ in the Beaufort Sea on 16-17 August 2010 (Figs. 10(a,b,c) and 11(a,e)). During the storm, waves and winds are oriented toward the North-West on the West side of the domain, but toward the West on the East side. Wave height and wind speed are reaching up to 3 m and 12 m/s (Fig. 10a,b), respectively, while they do not exceed 1 m and 7 m/s during the 3 days preceding the storm (not shown). Before the event, the south Beaufort Sea is ice-free, and the position of the sea ice edge (defined at the 15% sea ice concentration) is highly irregular, with the presence of an ice tongue centered around 72^{o}N and 155^{o}W, that is exposed upwind (and waves) on its eastern side but downwind on its western side during the storm. This sea ice tongue is composed of relatively thick ice ($\geq 1m$). During the storm, sea ice breaks all over the ice tongue in the western part of the domain, but not further than $\simeq$40 km after the sea ice edge. Both the waves and the wind stresses push the ice to the west (Fig. 10b,c), accelerating the drift that is directed north-west (Fig. 11a,c), as it was already the case before the storm (not shown). The wave action is particularly effective at the location of the sea ice tongue, where the WRS has an amplitude comparable to the wind stress over sea ice (Fig. 10c). As a consequence, the sea ice drift is substantially accelerated (Fig. 11c). Considering the effect of the waves results in large changes of the sea ice thickness pattern (when comparing the CPL and NOT_CPL runs), with a decrease on the eastern part of the tongue but an increase on the western part (Fig. 11g). Outside of the sea ice tongue, the differences between the simulations are very small, likely because of the sharp sea ice thickness gradient opposing internal resistance to deformation (Fig. 11e), and the relative small effect of the WRS compared to the wind stress (Fig. 10c).

The differences of sea ice properties around the sea ice tongue between the two runs also result in changes in SST and SSS, with increase around 1^{o}C and 1psu, respectively, on the eastern side of the sea ice tongue and a decrease of roughly the same magnitude on the western side (Fig. 12c,g). This differences arises from changes in sea ice melt, as differences of the total heat flux at the sea surface (Fig. 13a) are largely determined by bottom melt (Fig. 13b), the lateral melt contribution being one order of magnitude lower in this case. On the eastern side of the sea ice tongue, waves tend to push the sea ice away from the edge in the CPL run, and thus away from surface waters with warmer SST, resulting in a smaller amount of heat in the surface layer available for bottom melt. As the sea ice melt decreases, it also reduces the amount of freshwater received by the ocean surface, resulting in larger SSS. On the western side of the south end of the ice tongue, where the sea ice is thicker in the CPL run than in the NOT_CPL one, the opposite effect happens, eventually explaining the lower SST and SSS values. One should note that the effects of this storm are particularly strong, due to the specific conditions before the storm, with warm waters brought very close to the sea ice edge during the storm (not shown) .

In our model, bottom melt arises from heat fluxes determined by two distinct processes: (i) a conductive heat flux, which intensity is controlled by the difference between sea ice temperature and SST, and (ii) a turbulent heat flux in the surface layer, which depends on both the SST and the shear between the sea ice and the sea surface currents . The inclusion of the effect of the waves and the WRS could in principle modified the total bottom melt through its effect on the sea ice drift, but it is not the case here, suggesting that the deficit of sea ice melt on the eastern side of the sea ice tongue in the CPL run is therefore due to the combination of colder SST and the sea ice reduction.

4.2.2 Case 2: Storm in the Barents Sea (16-17 August 2010)

The storm that we just examined in the Beaufort Sea occurred on the same date than a second and stronger storm in the Barents Sea, with wave heights up to 5 m and south-westward winds reaching $\simeq$15m/s on average over the two days (bottom panels of Fig. 10d,e). In the CPL run, waves break-up sea ice over a very large area (Fig. 11f). Similarly to what we see in the Beaufort Sea, the mean direction of propagation of the waves aligns with the direction of the wind over the ice-free ocean, and is rotated orthogonally to the gradient in sea ice thickness once in the sea ice pack (Fig. 10d). The transition is however much smoother here than in the Beaufort Sea as the gradient is much weaker (Fig. 11f). In the CPL run, sea ice is drifting southward (Fig. 11b), with a slight deviation from the wind direction, and speeds twice larger than in the Beaufort Sea, due to stronger winds and thinner and less concentrated sea ice.

In contrast to the effect of the storm in the Beaufort Sea, the WRS in the CPL run reaches large values (Fig. 10f). Indeed, the strong storm generates very high waves of which attenuation induces WRS close to the sea ice edge as large as the wind stress, although the WRS does not align with the direction of the wave propagation in ice. This is due to the low sea ice concentration in this region that allows for wave generation on a large region, even if partially ice-covered. The attenuation of these short in-ice generated waves dominates the WRS that is therefore aligned with the wind direction, thus accelerating the ice drift, especially close to the ice edge (Fig. 11d).

The differences in sea ice drift between the CPL and the NOT_CPL runs also result in differences in bottom melt (Fig. 13d), and more specifically of the part associated with the turbulent heat flux (not shown). This increase of the turbulent heat flux, which occurs in the Barents Sea but not in the Beaufort Sea, can be explained by the larger ice drift velocities driven by the WRS, which intensify the shear between the sea ice and the ocean, and therefore the turbulence in the surface mixed layer. The differences in sea ice drift between the two runs also result in changes of the conductive heat flux. Yet, in the Barents Sea, the sea ice thickness and concentrations are lower than in the Beaufort Sea while the sea ice temperature is overall higher (not shown). This results in only moderate differences of the conductive heat flux between the CPL and the NOT_CPL runs.

The differences in SST and SSS exhibit similar pattern than the differences in heat flux (Fig. 12d,h and Fig. 13c), but the magnitude of the differences are much weaker than in the Beaufort Sea, not exceeding a few tenths of ^{o}C and psu for SST and SSS respectively. These small differences can be explained by two causes: (i) the small differences of sea ice properties between the two simulations result in small changes in melt, and (ii) the initial state before the storm is also different with higher SST and SSS in CPL (not shown). This difference in the initial state can be related to previous waves and wind conditions (not shown): low wind speeds are not sufficient to generate waves in the MIZ, implying that the WRS must be directed northward in the same direction as the propagating waves. It therefore compacts the sea ice edge, and thus reduces sea ice melt in the MIZ in the CPL run. As seen in the Beaufort Sea case, this in turn leads to higher SST and SSS values in the vicinity of the ice edge.

4.2.3 What determines the impact of the waves?

From these two particular cases we suggest a generalization of the mechanisms by which the waves can impact the sea ice and ocean properties in the MIZ. It is based on a simple principle: if sea ice is moved towards warmer water, it tends to melt more, and *vice versa*. The direction of the WRS compared to the orientation of the sea ice edge is thus fundamental if we are to understand the impact of the waves. In compact sea ice, waves are quickly attenuated and the direction of the WRS is generally towards the packed ice, thus impeding part of the sea ice melt and increasing the SST and SSS (Fig. 8). In regions where the sea ice is less concentrated and thinner, waves can be generated locally, so that the WRS aligns with the wind, whose direction determines the impact of the WRS (enhanced melt for off-ice wind and reduced melt for on-ice wind). Another key factor determining the impact of the WRS onto sea ice is the internal stress of sea ice (a.k.a the rheology; see Eq.2). The impact of the WRS is larger in regions of the MIZ where the sea ice is thin and low concentrated, as the internal stress tends to be negligible (Hibler III, 1979), making the sea ice easier to deform and to drift freely. Close to the sea ice edge in the Barents Sea for instance, the WRS in storm-induced high waves conditions can be larger than the wind stress, strongly accelerating the sea ice drift towards the open ocean, which also result in an increase of the ice/ocean shear, enhancing the turbulent heat flux under sea ice and the sea ice melt.

5 Discussion and conclusion

The goal of this study was to examine the wave-sea ice interactions in the MIZ of the Arctic Ocean during the melt season, as these processes are thought to be important for determining the sea ice conditions but are not accounted for in the state-of-the-art sea ice models. To that aim, we have developed a model framework, coupling the wave model WW3 with a modified version of the ocean/sea ice model NEMO-LIM3. The coupled model was then used to examine two aspects of the wave-sea ice interactions: (i) the impact of the WRS on the sea ice drift in the MIZ, and (ii) the effects of the wave-induced sea ice break-up on the sea ice melt. The WRS tends to compact the ice edge and thus reduces the total sea ice melt in the MIZ. Yet, its overall impact on the MIZ sea ice area and volume remains limited (Fig. 7b). However, it has a visible impact on sea ice drift velocity, accelerating it by $\simeq$9%. Compared to the use of Lüpkes et al. (2012) parameterization to estimate the floe size used in lateral melt, our parameterization strongly reduces the amount of sea ice melted laterally. It is however mostly compensated by an increase of bottom melt. As a result, the effects on sea ice and sea surface properties can be locally substantial, and even more substantial during storms, as illustrated by the case studies in the Beaufort and Barents seas. As the storminess in the Arctic region is expected to increase in the future (Day et al., 2018; Day and Hodges, 2018), generating higher and energetic waves more frequently (Khon et al., 2014), the wave-sea ice interactions might become a dominant signal controlling the dynamics of the MIZ.

In the MIZ, waves push sea ice as they are attenuated, modifying locally the position of the sea ice edge through a modulation of the magnitude and timing of the sea ice melt, which result in significant changes of the SST and SSS. Although the impact at the pan-Arctic scale remains limited, case studies of storms in the Barents and Beaufort seas shows that it can be locally and intermittently important. Results from our simple configuration have also revealed that the WRS could strongly modulate the position of the sea ice edge. Yet, except very locally in response to strong storms, the position of the pan-Arctic sea ice edge simulated by our realistic configuration appears to be insensitive to the effect of the wave. This is likely because the position of the sea ice edge in a ocean-sea ice model is primarily determined by the atmospheric forcing and the bulk formulae, and is in particular strongly tight to the position of the sea ice edge in the atmospheric reanalysis (Chevallier et al., 2017). The effect of the waves on sea ice simulated by our coupled model are likely underestimated, and should be re-assessed in future studies based on a fully coupled model that includes an atmospheric component.

We also have tested two parameterizations of the lateral melt, based on wave-induced break-up information or solely on a scaling between the size of the floes and the sea ice concentration, following Lüpkes et al. (2012). In both cases, the effect of the lateral melt remains limited as any change of lateral melt tends to be compensated by an opposite change of bottom melt. The effect might however become more important if longer simulations were performed. Indeed, Zhang et al. (2016) found that, over a year, the lateral melt could affect significantly the sea ice thickness. In their case, a FSD-based parameterization was used (similar to the one we introduced in our coupled model), but the effect of the wave-induced break-up on the FSD was only crudely parameterized, resulting in lateral melt in the central Arctic most likely over-estimated (as this is the case when using the parameterization of Lüpkes et al., 2012). Adding a FSD in their sea ice model, Roach et al. (2018b) found large impact on the sea ice concentration in the MIZ and sea ice thickness everywhere in the Arctic after 20 years of simulation, and suggested that the difference found in the central Arctic results from a redistribution of the heat used for lateral melt instead of bottom melt, similar to what happens in our model over a shorter timescale. One should also remember that the studies of Zhang et al. (2016) and Roach et al. (2018b) were aiming at representing the evolution of floes larger than 1000 m on long time scales, whereas we make the assumption that unbroken floes have an uniform floe size set to 1000 m in order to focus on the important processes for the wave-sea ice interactions. Therefore we do not expect any impact of the lateral melt in regions that are not impacted by waves.

Among the wave-sea ice interaction processes considered in this study, we found that the dynamical effect of the waves (the WRS) has a larger impact than the thermodynamical one (through the additional lateral source melt). Our simulations were however limited to only a few weeks during the melting season and it is unclear if that result would hold if longer timescales were considered. To make progress on this question, we would need to implement a parameterization that account for the re-freezing of the floes, through lateral growth and welding. A first parameterization of that kind has been very recently developed by Roach et al. (2018a). We also anticipate that running simulation over longer time period would highlight new impacts of the WRS. Indeed, observations have revealed that heat stored during melt season below the mixed layer can significantly affect the sea ice growth the following year (Jackson et al., 2010; Timmermans, 2015). In regions where the WRS contributes to reduce the ice melt, an excess of summer heat could likely accumulate under the mixed layer, possibly modulating the future evolution of the sea ice melt and growth. Recently, Smith et al. (2018) have for instance observed that a large amount of heat stored under the mixed layer could be released to melt sea ice during a storm. The significant changes of SST and SSS found locally over 37 days also highlight that wave-sea ice interactions should be considered when trying the forecast the Arctic sea ice conditions on short timescale (up to a few weeks), as these surface ocean changes can greatly affect melting and refreezing conditions.

The coupling developed in the present study marks a valuable new step toward an improved representation of waves and sea ice interactions in models, which might improve the representation of the dynamics of the MIZ. Yet, our coupling relies on a number of assumptions, which are most likely leading to an underestimation of the impact of the wave on the ocean and sea ice conditions. For instance, in our coupling, the sea ice rheology is unaffected by fragmentation, which is unlikely to be the case (McPhee, 1980). Moreover, the sea ice model used here does not retain any memory of the past sea ice conditions, while wave would most likely affect differently sea ice that has been previously broken (Langhorne et al., 1998). Developing a similar coupling using a model that consider a state variable accounting for the previous sea ice conditions (such as the state variable ‘damage’ included in the sea ice model neXtSIM (Rampal et al., 2016; Williams et al., 2017)) would probably reveal new mechanisms via which waves can modulate the ocean and sea ice conditions in the MIZ.

https://doi.org/10.5194/tc-2019-92
Preprint. Discussion started: 27 May 2019

Finally, the coupling we have developed here is also only considering the interactions between wave and sea ice, without any direct coupling with the ocean and the atmosphere. Yet, we know that wave dissipation would also likely impact the mixed layer, by enhancing turbulence (Couvelard et al., Submitted), and eventually modulate the rate of sea ice melt and formation (Martin and Kauffman, 1981; Rainville et al., 2011; Lee et al., 2012; Smith et al., 2018). Similarly, the effect of the waves is probably damped due to the lack of feedbacks with the atmosphere (Khon et al., 2014). Future coupling should include some of these features in order to fully capture the complexity of the MIZ dynamics.

Code and data availability. Will be made available before final submission

Appendix A: Floe size redistribution in the sea ice model LIM3

Here we provide the details of the calculation and implementation of the FSD, and in particular of the mechanical redistribution function Φ_m that accounts for processes such as sea ice fragmentation, lead opening, ridging, and rafting. Following Zhang et al. (2015), Φ_m can be divided into 3 terms as $\Phi_m = \Phi_o + \Phi_r + \Phi_f$ where Φ_o represents the creation of open water, Φ_r represents sea ice ridging and rafting, and Φ_f represents the wave-induced floes fragmentation. Here we compute Φ_o and Φ_r in a similar way to Zhang et al. (2015), assuming that all the floes of different sizes have the same ice thickness distribution, so that changes in sea ice concentration due to open water creation or ridging affects all floes equally. As a result, the shape of the FSD and its evolution are independent from these two terms.

Assuming that, in a given grid cell, sea ice fragmentation does not induce any change of the sea ice concentration, Φ_f can be written as (Zhang et al., 2015):

$$\Phi_f = -Q(D)g_D(D) + \int_0^\infty Q(D')\beta(D',D)g_D(D')dD' \tag{A1}$$

where D is the floe size, $Q(D)$ is a redistribution probability function characterizing which floes are going to be broken depending on their size, and $\beta(D',D)$ is a redistribution factor quantifying the fraction of sea ice concentration transferred from one floe size to another as break-up occurs. Φ_f is thus used to transfer sea ice concentration from large floes to smaller floes. To ensure the conservation of sea ice area during fragmentation, β must respect (Zhang et al., 2015):

$$\int_0^\infty \beta(D',D)dD = 1 \tag{A2}$$

In the absence of a wave model to simulate the sea state, Zhang et al. (2015) has defined β so that it redistributes uniformly the sea ice concentration of the large broken floes into the smaller floe sizes categories of the FSD. Their redistribution probability function $Q(D)$ thus assumes that a constant fraction of the sea ice cover is broken by waves during each break-up event. Their definition of $Q(D)$ also ensures that larger floes contribute more to the redistribution than smaller floes.

https://doi.org/10.5194/tc-2019-92
Preprint. Discussion started: 27 May 2019

In our coupled model, sea ice break-up is initially computed by WW3 (for details see Boutin et al., 2018), and accounts for the sea state variability. In WW3, the FSD resulting from wave-induced break-up is assumed to follow a truncated power-law between a minimum ($D_{\min}$) and a maximum ($D_{\max}$) floe size. For consistency, the FSD in LIM3 after a given break-up event must follow the same power-law, defined for D taken in $[D_{\min}\ D_{\max}]$ as:

$$P(D > D_*) = KD_*^{-\gamma}, K \in \mathbb{R} \tag{A3}$$

$$p(D) = -K\gamma D^{-\gamma-1} \tag{A4}$$

where $P(D > D_*)$ is the probability of having $D > D_*$, and $p(D)$ is the associated probability density. In WW3, a break-up event occurs if, firstly, waves with a wavelength λ applies a strain on sea ice greater than a given threshold, and secondly if $\lambda/2$ which is assumed to be the value of the new maximum floe size is lower than the current $D_{\max}$ value in the wave model (Dumont et al., 2011). Therefore, a break-up event in WW3 corresponds to a decrease of $D_{\max}$.

As detailed in section 3.2, we define a maximum floe size in LIM3, $D_{\max,\mathrm{LIM3}}$, that is compared to the value of the maximum floe size received from WW3, $D_{\max,\mathrm{WW3}}$. Initially, ice is unbroken and $D_{\max,\mathrm{LIM3}} = D_{\max,\mathrm{WW3}}$. If break-up has occurred in WW3, then we have $D_{\max,\mathrm{WW3}} < D_{\max,\mathrm{LIM3}}$. In this case, $D_{\max,\mathrm{LIM3}}$ must be updated to $D_{\max,\mathrm{WW3}}$ value, and Φ_f must be computed so that it forces the FSD in LIM3 to match the FSD assumed in WW3.

In practice in LIM3, we define a given number N of floe size categories, such that each floe size category $n \in [0, N]$ represents the floes with sizes in $[D_{n-1}, D_n]$. D_0 and D_N are the minimum and the maximum floe size possible in the model, respectively. D_N aims at representing floes that have not been broken by the waves. In WW3, the size of unbroken floes is set to 1000 m, and we thus also set D_N=1000m for consistency. Regarding the minimum floe size resulting from wave induced break-up, we set $D_{\min}$ to 8 m, which is the value of the minimum floe size used in the parameterization of lateral melt implemented in LIM3. This value is close to choices done in previous studies (see Williams et al., 2013; Bennetts et al., 2017). If break-up occurs, the update of $D_{\max,\mathrm{LIM3}}$ is done as follows:

$$\begin{cases} D_{n^*-1} < D_{\max,\mathrm{WW3}} \leq D_{n^*} \\ D_{\max,\mathrm{LIM3}} = D_{n^*}. \end{cases} \tag{A5}$$

To force the FSD to follow this power-law during the computation of the mechanical redistribution term Φ_f, in LIM3 we introduce changes in the computation of β and $Q(D)$. When using N floe size categories, the redistribution equation (A1) becomes:

$$\Phi_{f,n} = -Q_n g_n + \sum_{m=1}^{N} \beta(m,n) Q_m g_m \quad, m \in [0, N] \tag{A6}$$

Following Zhang et al. (2015), the redistribution factor $\beta(m,n)$ must respect Eq.A2. $\beta(m,n)$ should also allow to switch from completely unbroken ice to a truncated power-law distribution with lower limit D_0 and upper limit $D_{\max,\mathrm{LIM3}}$ if break-up occurs. $\beta(m,n)$ must finally ensure that floe size can only decrease during the fragmentation. To do so, $\beta(m,n)$ is defined as:

$$\begin{cases} \beta(m,n) = \dfrac{D_n^{2-\gamma} - D_{n-1}^{2-\gamma}}{\min(D_{n^*}, D_m)^{2-\gamma} - D_0^{2-\gamma}} \text{ if } m \geq n \text{ and } n \leq n^* \\ \beta(m,n) = 0 \text{ otherwise} \end{cases} \tag{A7}$$

With this choice of $\beta(m,n)$, the FSD of each floe size category $n < n^*$ is equal to the distribution function derived from the power-law assumed in WW3 ($g_{n,\mathrm{P.L}}$), given by:

$$g_{n,\mathrm{P.L}} = c\frac{\int_{D_{n-1}}^{D_n} D^2 p(D)dD}{\int_{D_0}^{D_{\max}} D^2 p(D)dD} = c\frac{D_n^{2-\gamma} - D_{n-1}^{2-\gamma}}{D_{\max}^{2-\gamma} - D_0^{2-\gamma}}, \tag{A8}$$

c being the sea ice concentration.

If sea ice in a given grid cell has already been broken, the FSD may have deviated from the truncated power-law distribution (due to advection or melting). If break-up occurs again at a latter model time step, we force the FSD to be reset to the power-law assumed in WW3, by adjusting the fraction of each floe size category contributing to the redistribution through the value Q_n. This ensures that the FSD in LIM3 and WW3 are identical. After a break-up event, $D_{\max,\mathrm{LIM3}}$ is the new maximum floe size in LIM3. The sea ice contained in floe size categories associated with floes larger than $D_{\max,\mathrm{LIM3}}$ is therefore entirely redistributed into smaller floe size categories by setting:

$$Q_n|_{n>n^*} = 1. \tag{A9}$$

The smallest floe size category (*i.e* $D \in [D_0, D_1]$) does not contribute to the floe size redistribution, assuming that this category accounts for floes too small to be broken by waves (Toyota et al., 2011). It therefore forces $Q_1 = 0$. For a given floe size category n, we define $\Delta g_{th,n}$ as the difference between the actual and theoretical values of the FSD for this floe size category ($\Delta g_{th,n}$ = $g_n - g_{n,\mathrm{P.L}}$, and the theoretical value is given by the truncated power-law between D_0 and $D_{\max,\mathrm{LIM3}}$). After the redistribution of floes between categories, $\Delta g_{th,n}$ needs to be zero, which is achieved through the adjustment of Q_n in order to obtain $\Phi_{f,n} = \Delta g_{th,n}$. The following system thus needs to be solved:

$$\begin{cases} \Phi_{f,2} = (-1+\beta_{2,2})Q_2 g_2 + \beta_{3,2}Q_3 g_3 + ... + \beta_{n^*,2}Q_{n^*}g_{n^*} + \sum\limits_{n>n^*}^{N} \beta_{n\geq n^*,2}g_n \\ \Phi_{f,3} = (-1+\beta_{3,3})Q_3 g_3 + \beta_{4,3}Q_4 g_4 + ... + \beta_{n^*,n^*}Q_{n^*}g_{n^*} + \sum\limits_{n>n^*}^{N} \beta_{n\geq n^*,3}g_n \\ \quad ... \\ \Phi_{f,n^*} = (-1+\beta_{n^*,n^*})Q_{n^*}g_{n^*} + \sum\limits_{n>n^*}^{N} \beta_{n\geq n^*,n^*}g_n, \end{cases} \tag{A10}$$

This system consists in a triangular matrix in which all diagonal terms are non-zero. It is solved by doing:

$$\begin{cases} Q_{n^*} = \max\left(0, \dfrac{\Delta g_{th,n^*} - \sum_{n>n^*}^{N} \beta_{n\geq n^*,n^*}g_n}{g_{n^*}(\beta_{n^*,n^*}-1)}\right) \\ ... \\ Q_2 = \max\left(0, \dfrac{\Delta g_{th,2} - \sum_{n>2}^{N} Q_n\beta_{n,2}g_n}{g_2(\beta_{2,2}-1)}\right) \end{cases} \tag{A11}$$

The constraint $Q_n > 0$ ensures that the redistribution can only be done toward categories containing smaller floe size. This constraint thus implies that, in the case where $\Delta g_{th,n} > 0$, the FSD in LIM3 is reset to the truncated power-law only if there is enough sea ice in large floes categories to be redistributed into smaller floes categories. Besides, setting $Q_1 = 0$ means that the sea ice concentration associated with the smallest floe size category is never redistributed. In the absence of lateral growth, a succession of break-up events leads to an accumulation of floes in this category, deviating the FSD from the theoretical power-law for floe sizes between D_0 and D_1 (see Fig. 3).

Competing interests. The authors declare no competing interests.

Acknowledgements. G.B. and F.A. are supported by DGA, ANR grants ANR-14-CE01-0012 MIMOSA, ANR-10-LABX-19-01, EU-FP7 project SWARP under grant agreement 607476, ONR grant number N0001416WX01117. Part of this work has been carried out as part of the Copernicus Marine Environment Monitoring Service (CMEMS) ArcticMix and WIzARd projects. CMEMS is implemented by Mercator Ocean in the framework of a delegation agreement with the European Union. We thank Martin Vancoppenolle for its valuable help as well as Verena Haid and Xavier Couvelard for their precious assistance in setting up the coupled framework.

https://doi.org/10.5194/tc-2019-92
Preprint. Discussion started: 27 May 2019

References

Aksenov, Y., Popova, E. E., Yool, A., Nurser, A. G., Williams, T. D., Bertino, L., and Bergh, J.: On the future navigability of Arctic sea routes: High-resolution projections of the Arctic Ocean and sea ice, Marine Policy, 75, 300–317, 2017.

Ardhuin, F., Sutherland, P., Doble, M., and Wadhams, P.: Ocean waves across the Arctic: attenuation due to dissipation dominates over scattering for periods longer than 19 s, Geophys. Res. Lett., 43, https://doi.org/10.1002/2016GL068204, 2016.

Ardhuin, F., Chapron, B., Collard, F., Smith, M., Stopa, J., Thomson, J., Doble, M., Wadhams, P., Blomquist, B., Persson, O., and Collins, III, C. O.: Measuring ocean waves in sea ice using SAR imagery: A quasi-deterministic approach evaluated with Sentinel-1 and in situ data, Remote Sensing of Environment, 189, 211–222, 2017.

Ardhuin, F., Boutin, G., Stopa, J., Girard-Ardhuin, F., Melsheimer, C., Thomson, J., Kohout, A., Doble, M., and Wadhams, P.: Wave Attenuation Through an Arctic Marginal Ice Zone on October 12, 2015: 2. Numerical modeling of Waves and Associated Ice Break-Up, Journal of Geophysical Research: Oceans, https://doi.org/10.1002/2018JC013784, 2018.

Asplin, M. G., Galley, R., Barber, D. G., and Prinsenberg, S.: Fracture of summer perennial sea ice by ocean swell as a result of Arctic storms, J. Geophys. Res., 117, C06 025, https://doi.org/10.1029/2011JC007221, 2012.

Barnier, B., Madec, G., Penduff, T., Molines, J.-M., Treguier, A.-M., Sommer, J. L., Beckmann, A., Biastoch, A., Böning, C., Dengg, J., Derval, C., Durand, E., Gulev, S., Remy, E., Talandier, C., Theetten, S., Maltrud, M., McClean, J., and Cuevas, B. D.: Impact of partial steps and momentum advection schemes in a global ocean circulation model at eddy-permitting resolution, Ocean Modelling, 56, 543–567, https://doi.org/10.1007/s10236-006-0082-1, 2006.

Bennetts, L., O'Farrell, S., and Uotila, P.: Brief communication: Impacts of ocean-wave-induced breakup of Antarctic sea ice via thermodynamics in a stand-alone version of the CICE sea-ice model, The Cryosphere, 11, 1035–1040, https://doi.org/10.5194/tc-11-1035-2017, 2017.

Boutin, G., Ardhuin, F., Dumont, D., Sévigny, C., Girard-Ardhuin, F., and Accensi, M.: Floe Size Effect on Wave-Ice Interactions: Possible Effects, Implementation in Wave Model, and Evaluation, Journal of Geophysical Research: Oceans, 123, 4779–4805, https://doi.org/10.1029/2017JC013622, 2018.

Brodeau, L., Barnier, B., Treguier, A.-M., Penduff, T., and Gulev, S.: An ERA40-based atmospheric forcing for global ocean circulation models, Ocean Modelling, 31, 88–104, 2010.

Cheng, S., Rogers, W. E., Thomson, J., Smith, M., Doble, M. J., Wadhams, P., Kohout, A. L., Lund, B., Persson, O. P., Collins, C. O., et al.: Calibrating a viscoelastic sea ice model for wave propagation in the arctic fall marginal ice zone, Journal of Geophysical Research: Oceans, 122, 8770–8793, 2017.

Chevallier, M., Smith, G. C., Dupont, F., Lemieux, J.-F., Forget, G., Fujii, Y., Hernandez, F., Msadek, R., Peterson, K. A., Storto, A., et al.: Intercomparison of the Arctic sea ice cover in global ocean–sea ice reanalyses from the ORA-IP project, Climate Dynamics, 49, 1107–1136, 2017.

Collins, III, C. O., Rogers, W. E., Marchenko, A., and Babanin, A. V.: In situ measurements of an energetic wave event in the Arctic marginal ice zone, Geophys. Res. Lett., 42, 1863–1870, https://doi.org/10.1002/2015GL063063, 2015.

Comiso, J. C., Meier, W. N., and Gersten, R.: Variability and trends in the Arctic Sea ice cover: Results from different techniques, Journal of Geophysical Research: Oceans, 2017.

Couvelard, X., Lemarié, F., Samson, G., Redelsperger, J.-L., Ardhuin, F., Benshila, R., and Madec, G.: Development of a 2-way coupled ocean-wave model: assessment on a global oceanic configuration, Geoscientific Model Development, Submitted.

Craig, A., Valcke, S., and Coquart, L.: Development and performance of a new version of the OASIS coupler, OASIS3-MCT_3. 0, Geoscientific Model Development, 10, 3297, 2017.

Day, J. J. and Hodges, K. I.: Growing land-sea temperature contrast and the intensification of Arctic cyclones, Geophysical Research Letters, 45, 3673–3681, 2018.

Day, J. J., Holland, M. M., and Hodges, K. I.: Seasonal differences in the response of Arctic cyclones to climate change in CESM1, Climate dynamics, 50, 3885–3903, 2018.

Dumont, D., Kohout, A., and Bertino, L.: A wave-based model for the marginal ice zone including a floe breaking parameterization, J. Geophys. Res., 116, C00E03, https://doi.org/10.1029/2010JC006682, 2011.

Dupont, F., Higginson, S., Bourdallé-Badie, R., Lu, Y., Roy, F., Smith, G., Lemieux, J., Garric, G., and Davidson, F.: A high-resolution ocean and sea-ice modelling system for the Arctic and North Atlantic oceans, Geoscientific Model Development, 8, 1577, 2015.

Feltham, D. L.: Granular flow in the marginal ice zone, Philosophical Transactions of the Royal Society of London A: Mathematical, Physical and Engineering Sciences, 363, 1677–1700, 2005.

Hibler III, W. D.: A Dynamic Thermodynamic Sea Ice Model, Journal of Physical Oceanography, 9, 815–846, https://doi.org/10.1175/1520-0485(1979)009<0815:ADTSIM>2.0.CO;2, 1979.

Horvat, C. and Tziperman, E.: A prognostic model of the sea-ice floe size and thickness distribution, The Cryosphere, 9, 2119–2134, https://doi.org/10.5194/tc-9-2119-2015, http://www.the-cryosphere.net/9/2119/2015/, 2015.

Inoue, J., Wakatsuchi, M., and Fujiyoshi, Y.: Ice floe distribution in the Sea of Okhotsk in the period when sea-ice extent is advancing, Geophysical research letters, 31, 2004.

Jackson, J., Carmack, E., McLaughlin, F., Allen, S. E., and Ingram, R.: Identification, characterization, and change of the near-surface temperature maximum in the Canada Basin, 1993–2008, Journal of Geophysical Research: Oceans, 115, 2010.

Khon, V., Mokhov, I., Pogarskiy, F., Babanin, A., Dethloff, K., Rinke, A., and Matthes, H.: Wave heights in the 21st century Arctic Ocean simulated with a regional climate model, Geophysical Research Letters, 41, 2956–2961, 2014.

Kohout, A. L., Williams, M. J. M., Dean, S. M., and Meylan, M. H.: Storm-induced sea-ice breakup and the implications for ice extent, Nature, 509, 604–607, https://doi.org/10.1038/nature13262, 2014.

Langhorne, P. J., Squire, V. A., Fox, C., and Haskell, T. G.: Break-up of sea ice by ocean waves, Annals of Glaciology, 27, 438–442, 1998.

Lee, C. M., Cole, S., Doble, M., Freitag, L., Hwang, P., Jayne, S., Jeffries, M., Krishfield, R., Maksym, T., and Maslowski, W.: Marginal Ice Zone (MIZ) program: Science and experiment plan, Tech. rep., WASHINGTON UNIV SEATTLE APPLIED PHYSICS LAB, 2012.

Lemieux, J.-F., Lei, J., Dupont, F., Roy, F., Losch, M., Lique, C., and Laliberté, F.: The Impact of Tides on Simulated Landfast Ice in a Pan-Arctic Ice-Ocean Model, Journal of Geophysical Research: Oceans, 123, 7747–7762, 2018.

Lique, C., Holland, M. M., Dibike, Y. B., Lawrence, D. M., and Screen, J. A.: Modeling the Arctic freshwater system and its integration in the global system: Lessons learned and future challenges, Journal of Geophysical Research: Biogeosciences, 121, 540–566, 2016.

Longuet-Higgins, M. S.: The mean forces exerted by waves on floating or submerged bodies with applications to sand bars and wave power machines, Proc. Roy. Soc. Lond. A, 352, 463–480, 1977.

Longuet-Higgins, M. S. and Stewart, R. W.: Radiation stresses and mass transport in surface gravity waves with application to 'surf beats', J. Fluid Mech., 13, 481–504, 1962.

Lüpkes, C., Gryanik, V. M., Hartmann, J., and Andreas, E. L.: A parametrization, based on sea ice morphology, of the neutral atmospheric drag coefficients for weather prediction and climate models, Journal of Geophysical Research: Atmospheres, 117, 2012.

Madec, G.: NEMO ocean engine, Note du Pôle de modélisation, Institut Pierre-Simon Laplace (IPSL), France, No 27, ISSN No 1288-1619, 2008.

Marcq, S. and Weiss, J.: Influence of sea ice lead-width distribution on turbulent heat transfer between the ocean and the atmosphere, The Cryosphere, 6, 143–156, 2012.

Martin, S. and Kauffman, P.: A Field and Laboratory Study of Wave Damping by Grease Ice, Journal of Glaciology, 27, 283–313, https://doi.org/10.1017/S0022143000015392, 1981.

Maykut, G. A. and Perovich, D. K.: The role of shortwave radiation in the summer decay of a sea ice cover, Journal of Geophysical Research: Oceans, 92, 7032–7044, 1987.

McPhee, M. G.: An analysis of pack ice drift in summer, Sea ice processes and models, pp. 62–75, 1980.

Montiel, F., Squire, V. A., and Bennetts, L. G.: Attenuation and directional spreading of ocean wave spectra in the marginal ice zone, J. Fluid Mech., 790, 492–522, https://doi.org/10.1017/jfm.2016.2, 2016.

Perrie, W. and Hu, Y.: Air–ice–ocean momentum exchange. Part II: Ice drift, Journal of physical oceanography, 27, 1976–1996, 1997.

Rainville, L., Lee, C. M., and Woodgate, R. A.: Impact of wind-driven mixing in the Arctic Ocean, Oceanography, 24, 136–145, 2011.

Rampal, P., Bouillon, S., Olason, E., and Morlighem, M.: neXtSIM: a new Lagrangian sea ice model, CRYOSPHERE, 10, https://doi.org/10.5194/tc-10-1055-2016, 2016.

Roach, L. A., Horvat, C., Dean, S. M., and Bitz, C. M.: An emergent sea ice floe size distribution in a global coupled ocean–sea ice model, Journal of Geophysical Research: Oceans, 2018a.

Roach, L. A., Smith, M. M., and Dean, S. M.: Quantifying growth of pancake sea ice floes using images from drifting buoys, Journal of Geophysical Research: Oceans, 2018b.

Rogers, W. E., Thomson, J., Shen, H. H., Doble, M. J., Wadhams, P., and Cheng, S.: Dissipation of wind waves by pancake and frazil ice in the autumn Beaufort Sea, J. Geophys. Res., 121, https://doi.org/10.1002/2016JC012251, 2016.

Rothrock, D. and Thorndike, A.: Measuring the sea ice floe size distribution, Journal of Geophysical Research: Oceans, 89, 6477–6486, 1984.

Rousset, C., Vancoppenolle, M., Madec, G., Fichefet, T., Flavoni, S., Barthélemy, A., Benshila, R., Chanut, J., Lévy, C., Masson, S., et al.: The Louvain-La-Neuve sea ice model LIM3. 6: global and regional capabilities, Geoscientific Model Development, 8, 2991, 2015.

Shen, H. H. and Ackley, S. F.: A one-dimensional model for wave-induced ice-floe collisions, Annals of Glaciology, 15, 87–95, 1991.

Smith, M., Stammerjohn, S., Persson, O., Rainville, L., Liu, G., Perrie, W., Robertson, R., Jackson, J., and Thomson, J.: Episodic reversal of autumn ice advance caused by release of ocean heat in the Beaufort Sea, Journal of Geophysical Research: Oceans, 2018.

Squire, V. A.: A fresh look at how ocean waves and sea ice interact, Phil. Trans. R. Soc. A, 376, 20170 342, 2018.

Steele, K., Teng, C.-C., and Wang, D. W.-C.: Wave direction measurements using pitch and roll buoys, Ocean Eng., 19, 349–375, 1992.

Steele, M.: Sea ice melting and floe geometry in a simple ice-ocean model, Journal of Geophysical Research: Oceans, 97, 17 729–17 738, https://doi.org/10.1029/92JC01755, 1992.

Steele, M., Morison, J. H., and Untersteiner, N.: The partition of air-ice-ocean momentum exchange as a function of ice concentration, floe size, and draft, Journal of Geophysical Research: Oceans, 94, 12 739–12 750, 1989.

Stopa, J., Ardhuin, F., Thomson, J., Smith, M. M., Kohout, A., Doble, M., and Wadhams, P.: Wave Attenuation Through an Arctic Marginal Ice Zone on 12 October, 2015: 1. Measurement of Wave Spectra and Ice Features From Sentinel-1A, Journal of Geophysical Research: Oceans, 2018a.

Stopa, J. E., Ardhuin, F., and Girard-Ardhuin, F.: Wave climate in the Arctic 1992-2014: seasonality and trends, The Cryosphere, 10, 1605–1629, https://doi.org/10.5194/tc-10-1605-2016, 2016a.

Stopa, J. E., Ardhuin, F., Husson, R., Jiang, H., Chapron, B., and Collard, F.: Swell dissipation from 10 years of Envisat ASAR in wave mode, Geophys. Res. Lett., 43, 3423–3430, https://doi.org/10.1002/2015GL067566, 2016b.

Stopa, J. E., Sutherland, P., and Ardhuin, F.: Strong and highly variable push of ocean waves on Southern Ocean sea ice, Proceedings of the National Academy of Sciences, 115, 5861–5865, 2018b.

Stroeve, J., Hamilton, L. C., Bitz, C. M., and Blanchard-Wrigglesworth, E.: Predicting September sea ice: Ensemble skill of the SEARCH Sea Ice Outlook 2008-2013, Geophys. Res. Lett., 41, 2411–2418, https://doi.org/10.1002/2014GL059388, 2014.

Strong, C. and Rigor, I. G.: Arctic marginal ice zone trending wider in summer and narrower in winter, Geophysical Research Letters, 40, 4864–4868, https://doi.org/10.1002/grl.50928, 2013.

Sutherland, P. and Dumont, D.: Marginal ice zone thickness and extent due to wave radiation stress., Journal of Physical Oceanography, 2018.

Sutherland, P. and Melville, W. K.: Field measurements and scaling of ocean surface wave-breaking statistics, Geophys. Res. Lett., 40, 3074–3079, https://doi.org/10.1002/grl.50584, 2013.

The WAVEWATCH III® Development Group: User manual and system documentation of WAVEWATCH III ® version 5.16, Tech. Note 329, NOAA/NWS/NCEP/MMAB, College Park, MD, USA, 326 pp. + Appendices, 2016.

Thomson, J. and Rogers, W. E.: Swell and sea in the emerging Arctic Ocean, Geophys. Res. Lett., 41, 3136–3140, https://doi.org/10.1002/2014GL059983, 2014.

Thomson, J., Ackley, S., Girard-Ardhuin, F., Ardhuin, F., Babanin, A., Bidlot, J., Boutin, G., Brozena, J., Cheng, S., Doble, M., et al.: Overview of the arctic sea state and boundary layer physics program, Journal of Geophysical Research: Oceans, 2018.

Timmermans, M.-L.: The impact of stored solar heat on Arctic sea ice growth, Geophysical Research Letters, 42, 6399–6406, 2015.

Toyota, T., Haas, C., and Tamura, T.: Size distribution and shape properties of relatively small sea-ice floes in the Antarctic marginal ice zone in late winter, Deep Sea Research Part II: Topical Studies in Oceanography, 58, 1182–1193, 2011.

Uotila, P., Goosse, H., Haines, K., Chevallier, M., Barthélemy, A., Bricaud, C., Carton, J., Fučkar, N., Garric, G., Iovino, D., et al.: An assessment of ten ocean reanalyses in the polar regions, Climate Dynamics, pp. 1–38, 2018.

Vancoppenolle, M., Fichefet, T., Goosse, H., Bouillon, S., Madec, G., and Maqueda, M. A. M.: Simulating the mass balance and salinity of Arctic and Antarctic sea ice. 1. Model description and validation, Ocean Modelling, 27, 33–53, 2009.

Wang, Q., Ilicak, M., Gerdes, R., Drange, H., Aksenov, Y., Bailey, D. A., Bentsen, M., Biastoch, A., Bozec, A., Böning, C., et al.: An assessment of the Arctic Ocean in a suite of interannual CORE-II simulations. Part II: Liquid freshwater, Ocean Modelling, 99, 86–109, 2016.

Williams, T. D., Bennetts, L. G., Squire, V. A., Dumont, D., and Bertino, L.: Wave-ice interactions in the marginal ice zone. Part 2: Numerical implementation and sensitivity studies along 1D transects of the ocean surface, Ocean Modelling, 71, 92–101, https://doi.org/10.1016/j.ocemod.2013.05.011, 2013.

Williams, T. D., Rampal, P., and Bouillon, S.: Wave-ice interactions in the neXtSIM sea-ice model, The Cryosphere Discussions, pp. 1–28, https://doi.org/10.5194/tc-2017-24, 2017.

Zhang, J., Schweiger, A., Steele, M., and Stern, H.: Sea ice floe size distribution in the marginal ice zone: Theory and numerical experiments: Modeling floe size distribution, Journal of Geophysical Research: Oceans, 120, 3484–3498, https://doi.org/10.1002/2015JC010770, 2015.

Zhang, J., Stern, H., Hwang, B., Schweiger, A., Steele, M., Stark, M., and Graber, H. C.: Modeling the seasonal evolution of the Arctic sea ice floe size distribution, Elementa, 4, https://doi.org/10.12952/journal.elementa.000126, 2016.

Zhao, J., Barber, D., Zhang, S., Yang, Q., Wang, X., and Xie, H.: Record low sea-ice concentration in the central Arctic during summer 2010, Advances in Atmospheric Sciences, 35, 106–115, 2018.

https://doi.org/10.5194/tc-2019-92
Preprint. Discussion started: 27 May 2019

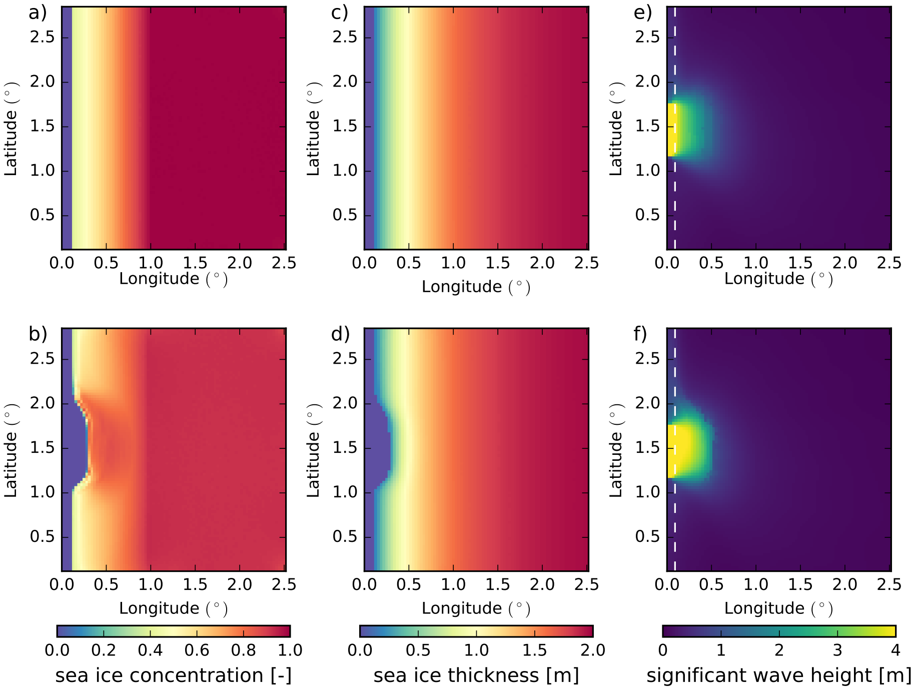

Figure 1. Implementation of the WRS in the idealized configuration. (a) and (c) show the initial state of sea ice concentration and thickness, respectively. (b) and (d) show sea ice concentration and thickness after 72 h in the WW3-LIM3 coupled model. (e) and (f) show the significant wave height Hs distribution after 72 h in the WW3 model and in the WW3-LIM3 coupled model, respectively. The white dashed line on (e) and (f) indicates the position of the ice edge (c=0.15).

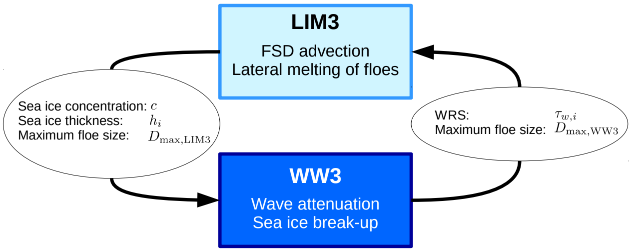

Figure 2. Schematic summarizing the exchanged information between the sea ice model LIM3 and the wave model WAVEWATCH III® in our coupled framework. The two boxes corresponds to the processes accounted for in a given model, while the variables exchanged between the models are listed in the bubbles.

.

https://doi.org/10.5194/tc-2019-92
Preprint. Discussion started: 27 May 2019

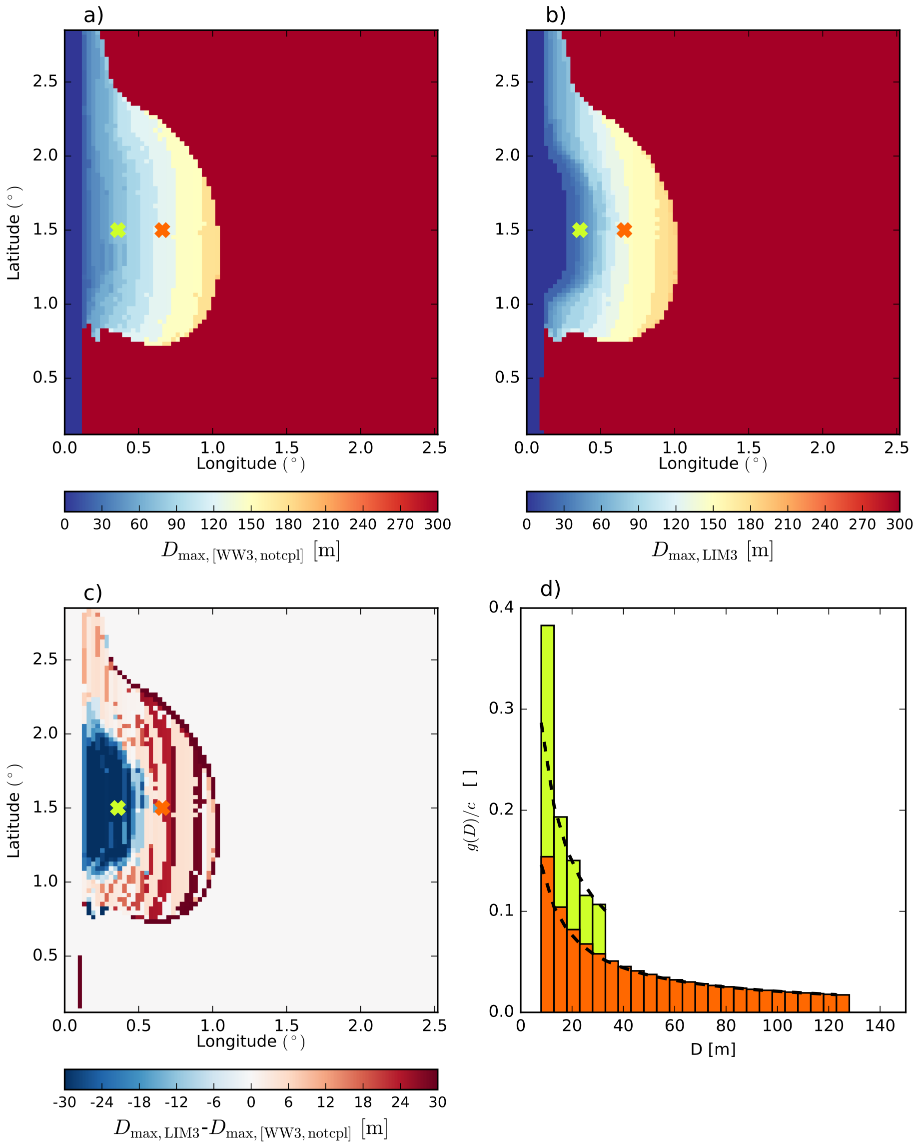

Figure 3. Snapshots of D_{max} from the WW3 (a) and the WW3-LIM3 (b) simulations after 72 h, and the difference between the two (c). Panel (d) shows the FSD from the WW3-LIM3 run at two locations indicated with crosses on panels a,b,c. The black dashed line in (d) corresponds to the theoretical power-law FSD assumed in WW3.

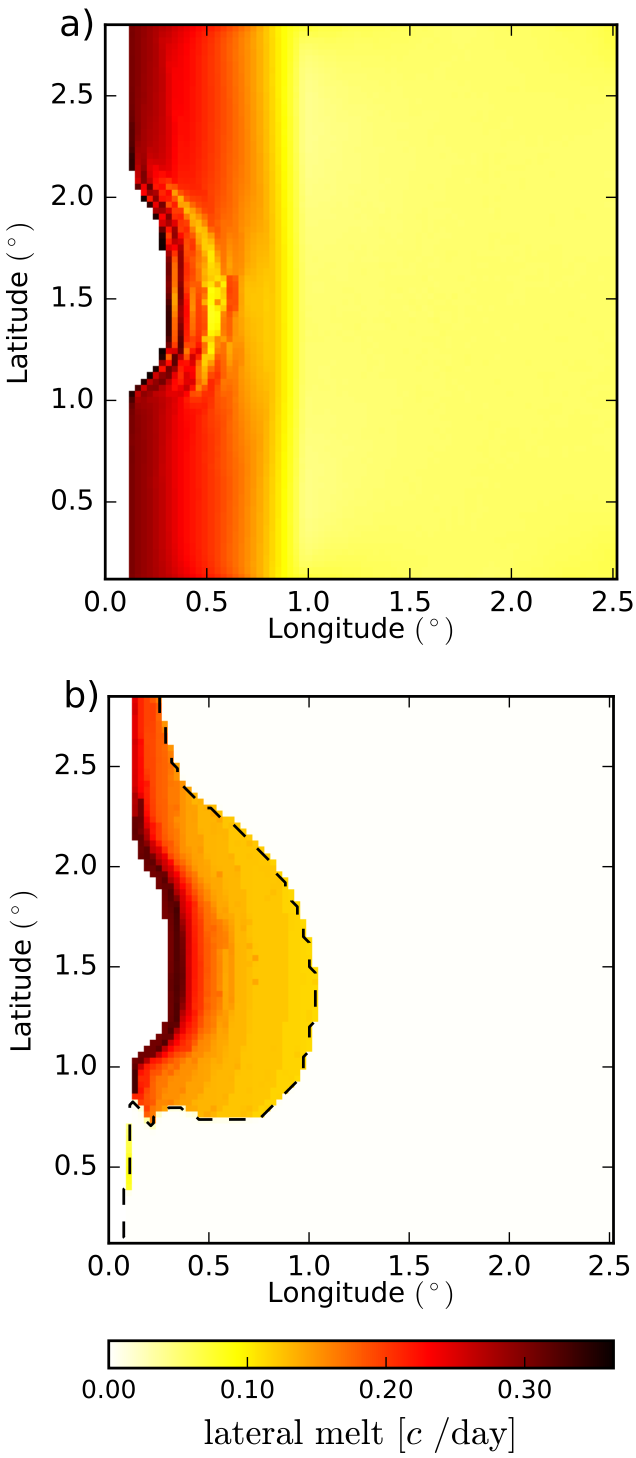

Figure 4. Lateral melt rates [estimated as percentage of sea ice concentration lost per day] estimated by the coupled model after 72 h of simulation using the parameterization of Lüpkes et al. (2012) (a), or the parameterization developed in this study accounting for wave-induced sea ice break-up (b). The black dashed contour on panel (b) indicates $D_{\max} = 500\ m$, and thus represents the limit between broken and unbroken sea ice.

https://doi.org/10.5194/tc-2019-92
Preprint. Discussion started: 27 May 2019

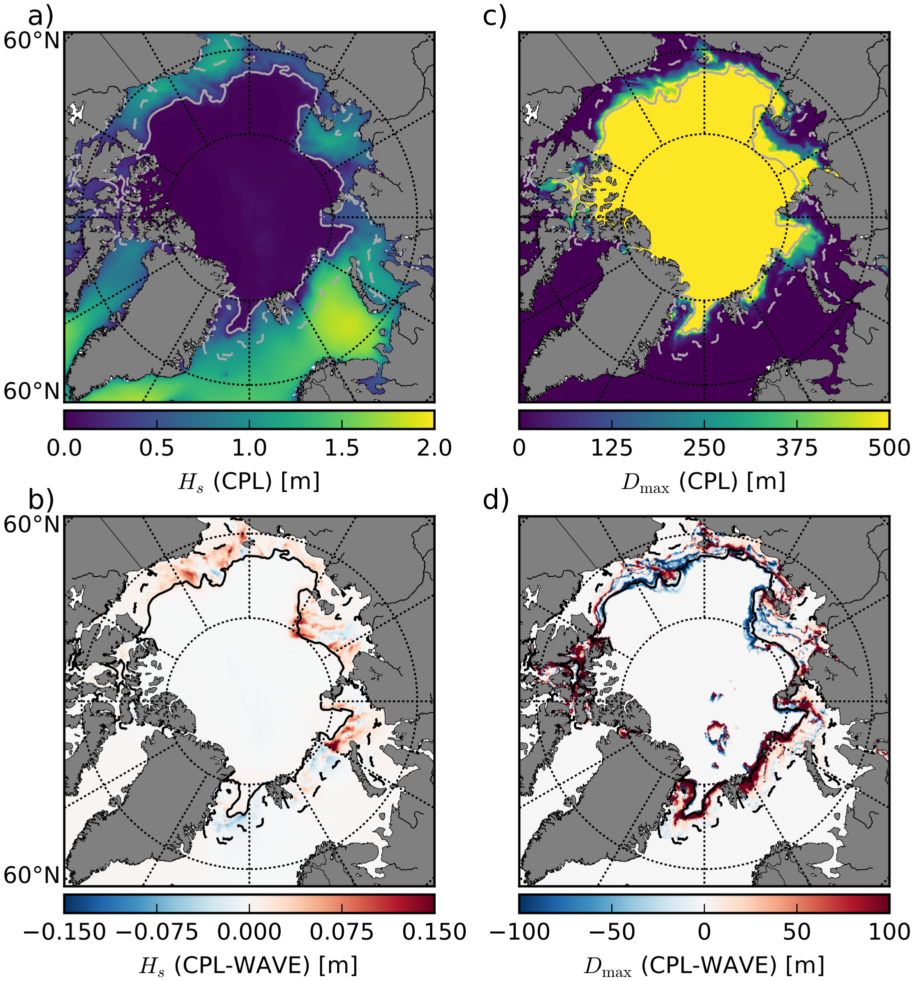

Figure 5. Significant wave height (a) and maximum floe size (c) in the CPL simulation averaged over the period 03-08-2010 to 09-09-2018, and the differences with the WAVE simulations (b, d). The black contours delimit the MIZ in the CPL simulation, defined here as $0 < \langle D_{\max} \rangle < 700$ m. Note that the sea ice conditions from the NOT_CPL run are used as forcing for the WAVE run and are thus similar in the WAVE and the NOT_CPL runs.

https://doi.org/10.5194/tc-2019-92
Preprint. Discussion started: 27 May 2019

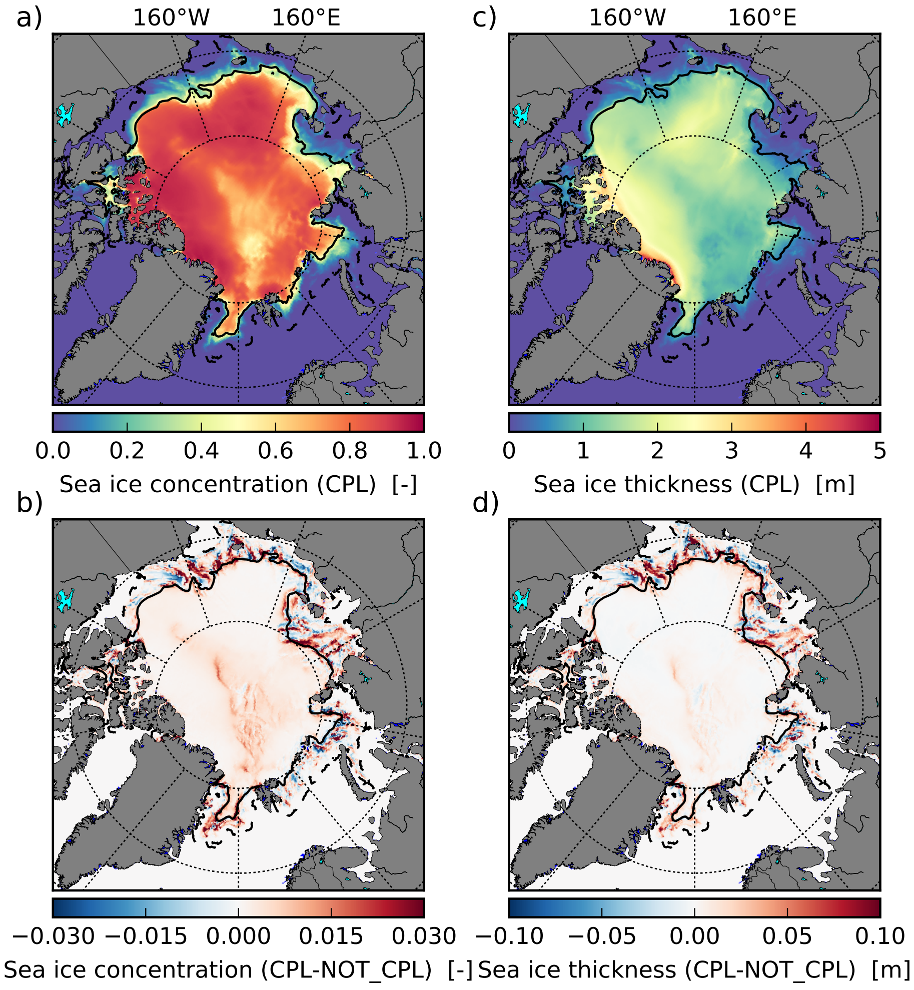

Figure 6. Sea ice concentration and thickness in the CPL simulation (a, c) and the difference with NOT_CPL (b,d) averaged over the period 04/08/2010 to 09/09/2010. The black contours delimit the MIZ in the CPL simulation, defined here as $0 < \langle D_{\max} \rangle < 700$ m.

https://doi.org/10.5194/tc-2019-92
Preprint. Discussion started: 27 May 2019

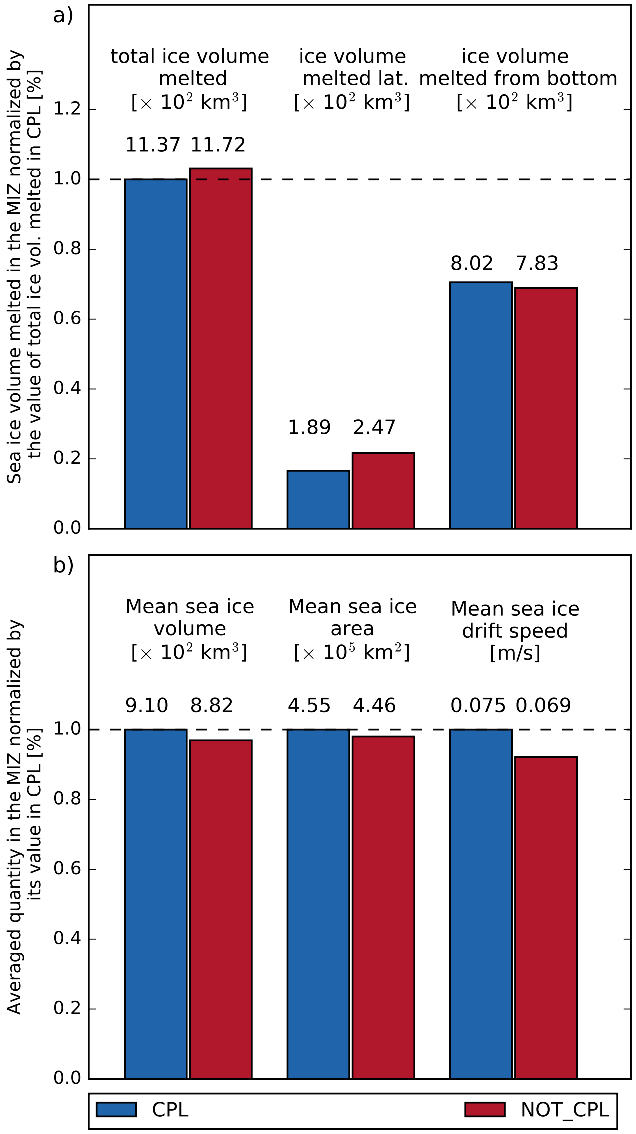

Figure 7. (a) Sea ice volume melted integrated over the MIZ and over the period between 04/08/2010 and 09/09/2010 in the CPL and the NOT_CPL simulations. Here the MIZ is defined as the region where $0 < \langle D_{\max} \rangle < 700$ m in the CPL run. The contribution from lateral melt and bottom melt to the total melt for both simulations are also represented. (b) Mean sea ice volume, area and drift speed in the MIZ over the same period.

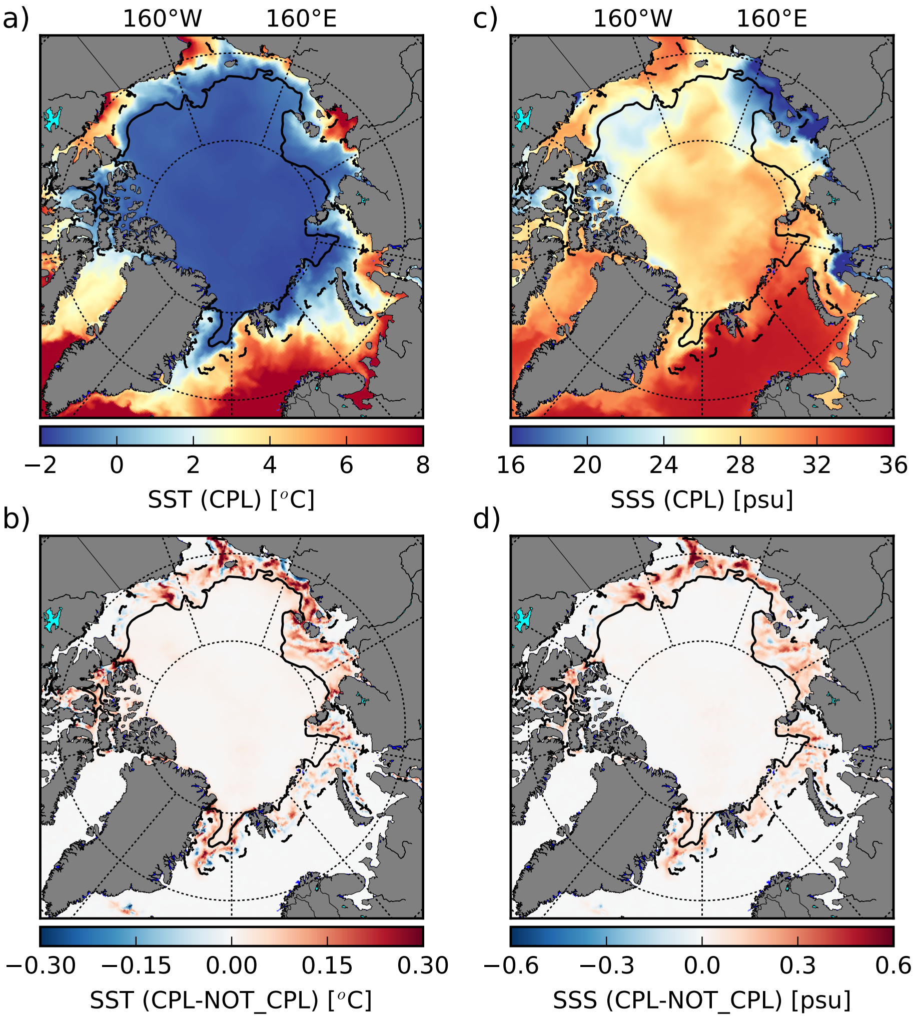

Figure 8. SST (a) and SSS (c) in the CPL run for the period between between 04/08/2010 and 09/09/2010,and the difference with NOT_CPL (b,d). The black contours delimit the MIZ in the CPL simulation, defined here as $0 < \langle D_{\max} \rangle < 700$ m.

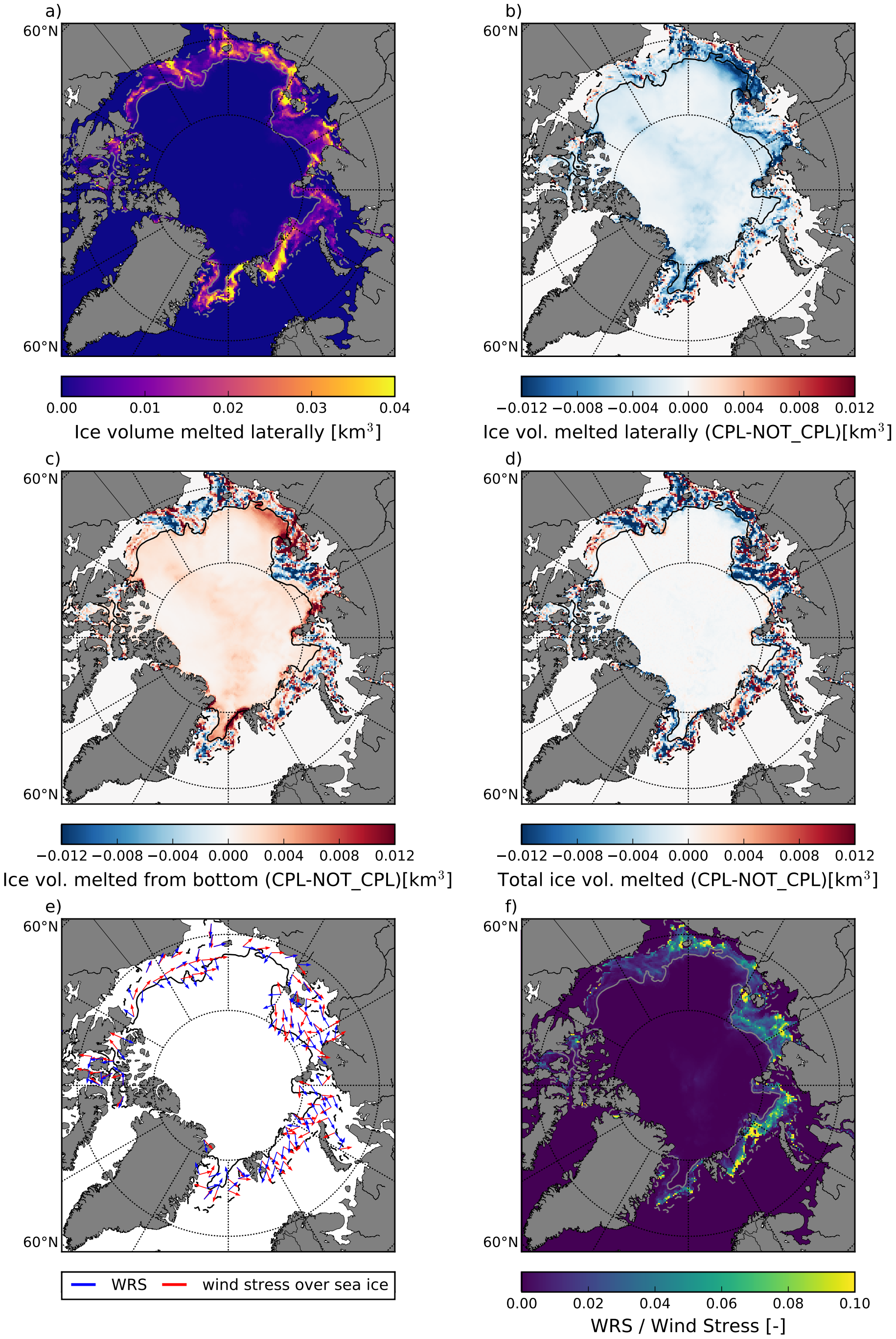

Figure 9. Volume of sea ice melted by lateral melt in the CPL simulation over the period between 04/08/2010 and 09/09/2010 (a). Differences between the CPL and the NOT_CPL runs of lateral melt (b), bottom melt (c) and total melt (d). (e) Wind stress (red) and WRS (blue) averaged over the same period 04/08/2010 and 09/09/2010 in the CPL simulation. Note that the WRS has been multiplied by a factor of 10 in order to improve readability. (f) Distribution of the relative magnitude of WRS over the wind stress. The grey contours represent the position of the ice edge ($c = 0.15$) on the first (solid line) and last day (dashed line) of the period considered in the CPL simulation.

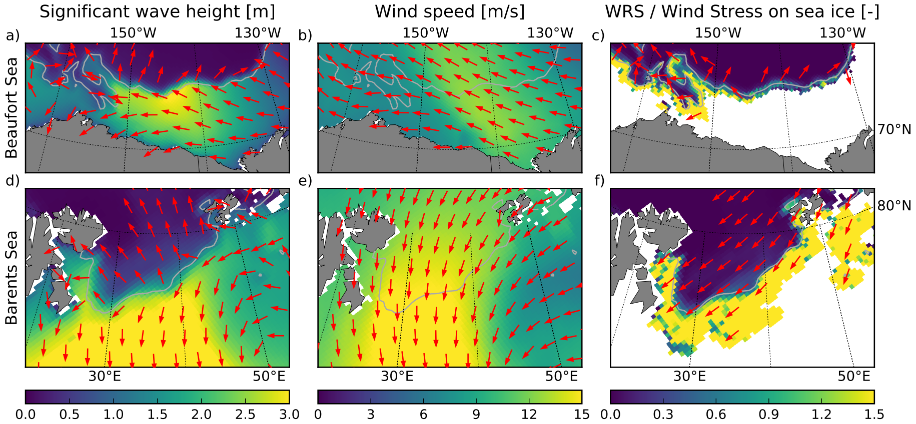

Figure 10. Significant wave height and wave mean direction of propagation (a, d), wind speed (b, e) and WRS (c, f) simulated by the CPL run during the storms that occurred in the Beaufort Sea (a, b, c) and in the Barents Sea (d, e, f) on 16/08/2010-17/08/2010. The grey contours indicate the position of the sea ice edge determined from the averaged sea ice concentration ($c = 0.15$).

https://doi.org/10.5194/tc-2019-92
Preprint. Discussion started: 27 May 2019

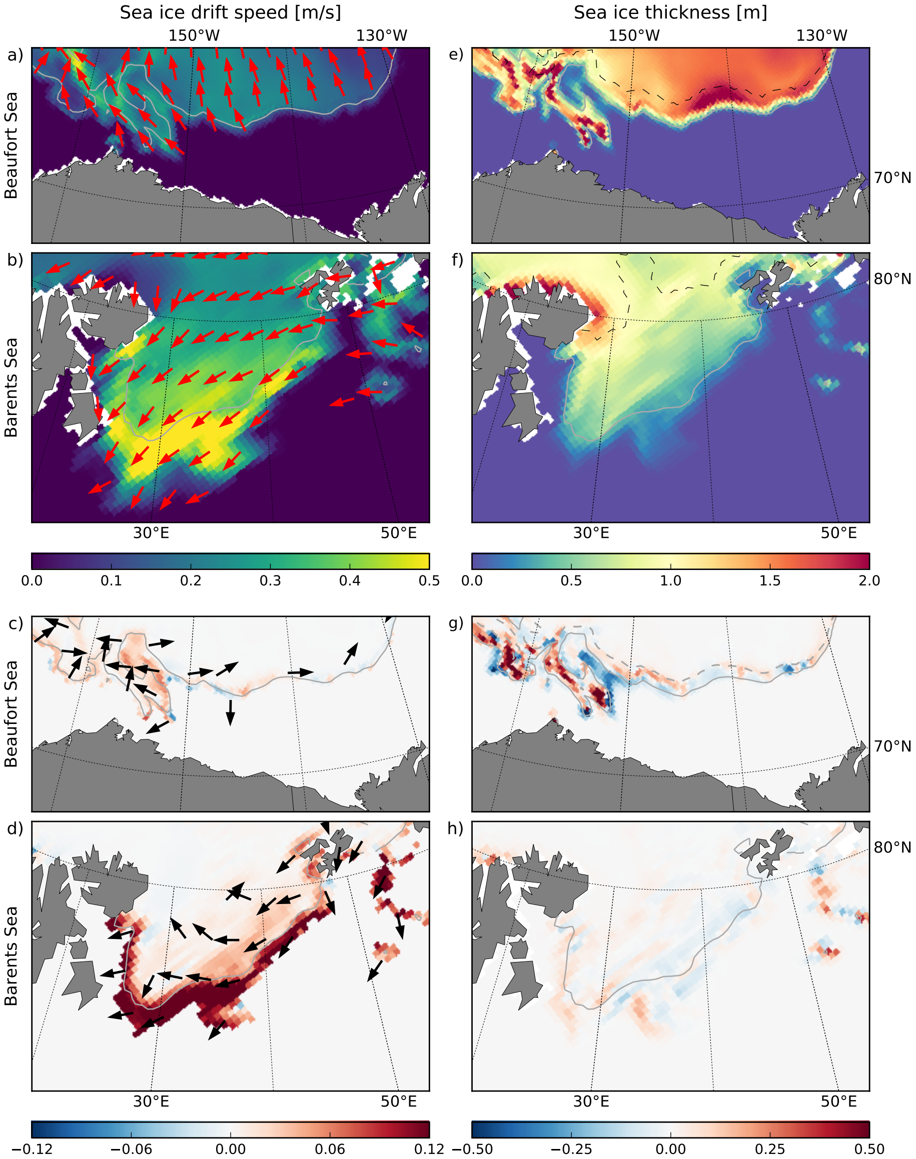

Figure 11. Mean sea ice drift (a, b) and sea ice thickness (e, f) simulated by the CPL run during the storms that occurred in the Beaufort Sea (a, c) and in the Barents Sea (b, f) on 16/08/2010-17/08/2010. Panels (c, d, g, h) show the differences for these quantities between the CPL and NOT_CPL simulations. Grey contours indicate the position of the ice edge determined from the averaged sea ice concentration ($c = 0.15$). The black dashed contour delimits the border between broken and unbroken ice ($D_{\max} = 500$m)

https://doi.org/10.5194/tc-2019-92
Preprint. Discussion started: 27 May 2019

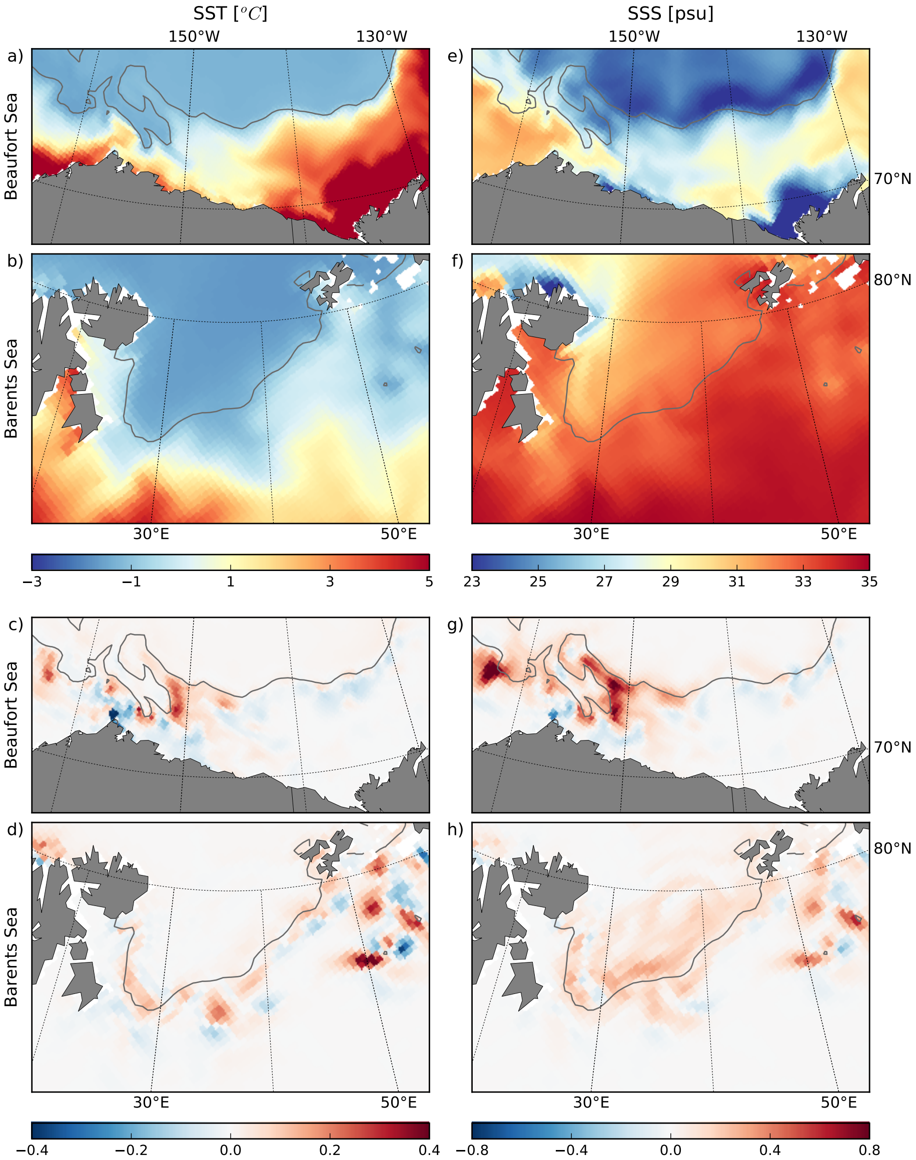

Figure 12. SST (a, b) and SSS (e, f) simulated by the CPL run during the storms that occurred in the Beaufort Sea (a, c) and in the Barents Sea (b, f) on 16/08/2010-17/08/2010. Panels (c, d, g, h) show the differences for these quantities between the CPL and NOT_CPL simulations. Grey contours indicate the position of the ice edge determined from the averaged sea ice concentration ($c = 0.15$).

https://doi.org/10.5194/tc-2019-92
Preprint. Discussion started: 27 May 2019

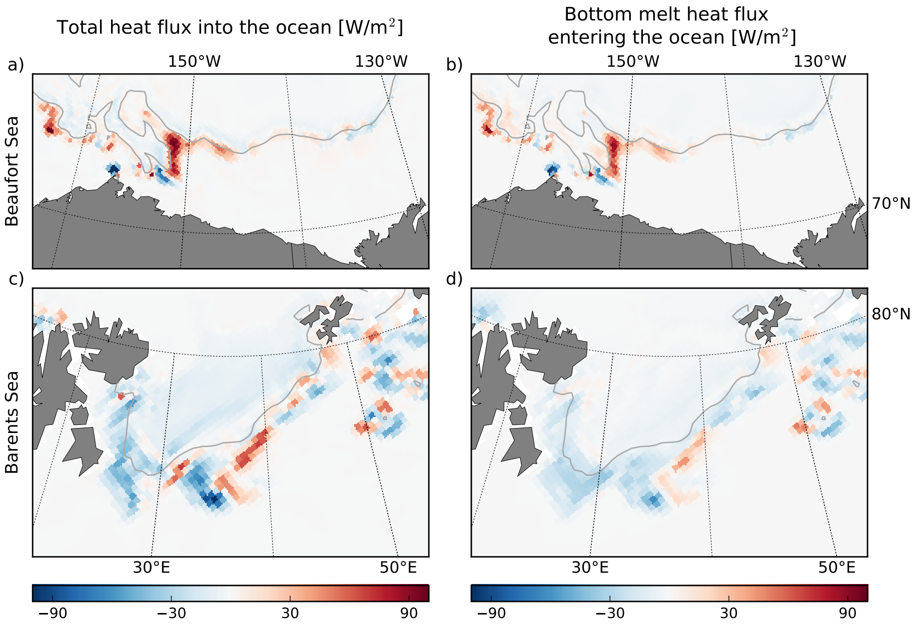

Figure 13. Averaged differences between the CPL and NOT_CPL simulations of (a, c) the heat flux into the ocean and (b, d) the contribution to the heat flux into the ocean coming from the sea ice bottom melt during the storms in the Beaufort Sea (a, b) and in the Barents Sea (c, d) which occurred on 16/08/2010-17/08/2010. Grey contours indicate the position of the ice edge determined from the averaged sea ice concentration ($c = 0.15$).